Bimodal mesoporous hard carbons from stabilized resorcinol-formaldehyde resin and silica template with enhanced adsorption capacity

Eduardo Fuentes-Quezada, Ezequiel de la Llave, Emilia Halac, Matías Jobbágy, Federico A. Viva, Mariano M. Bruno, Horacio R. Corti

PII: S1385-8947(18)32469-0
DOI: https://doi.org/10.1016/j.cej.2018.11.235
Reference: CEJ 20537

To appear in: *Chemical Engineering Journal*

Received Date: 28 August 2018
Revised Date: 15 November 2018
Accepted Date: 30 November 2018

Please cite this article as: E. Fuentes-Quezada, E. de la Llave, E. Halac, M. Jobbágy, F.A. Viva, M.M. Bruno, H.R. Corti, Bimodal mesoporous hard carbons from stabilized resorcinol-formaldehyde resin and silica template with enhanced adsorption capacity, *Chemical Engineering Journal* (2018), doi: https://doi.org/10.1016/j.cej.2018.11.235

Bimodal mesoporous hard carbons from stabilized resorcinol-formaldehyde resin and silica template with enhanced adsorption capacity

Eduardo Fuentes-Quezada[a], Ezequiel de la Llave[b], Emilia Halac[a], Matías Jobbágy[b], Federico A. Viva[a], Mariano M. Bruno[a,1,*], Horacio R. Corti[a,b,*]

[a]Departamento de Física de la Materia Condensada, Comisión Nacional de Energía Atómica, Avda. General Paz 1499 (1650), San Martín, Buenos Aires, Argentina.

[b]Instituto de Química Física de los Materiales, Medio Ambiente y Energía (INQUIMAE-CONICET), Facultad de Ciencias Exactas y Naturales, Universidad de Buenos Aires, Pabellón II, Ciudad Universitaria, (1428), Buenos Aires, Argentina.

KEYWORDS: Hard Carbon, Bimodal Pore Size Distribution, pDADMAC, Porous Silica, Adsorption Capacity.

[1]Present address: Departamento de Química, Universidad Nacional de Río Cuarto-CONICET, Ruta 8 y 36 Km 601, Río Cuarto, Córdoba, Argentina.

Corresponding authors.

Tel.: +54 358 4676157; Fax: +54 358 4676233. e-mail address: mbruno@exa.unrc.edu.ar. (M.M. Bruno).

Tel.: +54 11 67727174; Fax: +54 11 67727121. e-mail address: hrcorti@tandar.cnea.gov.ar. (H.R. Corti).

ABSTRACT

Hard carbon powders with hierarchical mesoporous structure from resorcinol-formaldehyde polymer were successfully prepared by use of double pore forming method. Poly-diallyldimethylammonium chloride (pDADMAC) and commercial silica (Sipernat® 50) were used as structuring agent and hard template, respectively. Through the proposed procedure carbon powder with bimodal mesoporous size distribution (around 4-5 nm and 20-40 nm) and different pore volume ratios can be obtained, by changing the ratio pDADMAC/silica used in the synthesis. Pore volumes between 0.70 and 2.10 $cm^3 \cdot g^{-1}$, and specific surface areas between 662 to 998 $m^2 \cdot g^{-1}$ were obtained.

Raman spectroscopy and X-Ray diffraction analysis showed that all the carbons presented a non-ordered mesopore structure, and a hard carbon micro-structure with roughly 40 % of single-layer microstructures, an average of 2.6 stacked graphene layers, and an in-plane graphitic crystallite size around 3.4 nm. We have evaluated the adsorption of methylene blue, as a model of a pollutant dye, on the mesoporous carbons with different pore size distribution, and we found that carbons with bimodal pore size distribution exhibit a remarkable and irreversible adsorption capacity. Microporosity can help to enhance the adsorption capacity, provided that micropores are connected to mesopores, allowing the adsorbate to get deep into the carbon structure. The adsorption kinetic is very fast for carbons with such pore architecture, and can be well described by a three-stage intraparticle diffusion model.

1. INTRODUCTION

Structured porous carbon materials are attracting widespread interest across several fields of nanotechnology [1]. The wide applicability can be attributed to their unique properties, high chemical and thermal stability, good electrical conductivity, intrinsic hydrophobicity, and facile modification of surface chemistry. Also, the tunability of nanostructure, morphology and pore size has been paramount for the developing of carbon materials for several applications [2,3]. Regarding storage energy applications, porous carbon containing parallel stacking of graphene layers (hard carbon), and a significant amount of nanoporosity, appears as promising anode material for energy storage devices such as Na-ion [4,5], and Li-O_2 [6] batteries. Mesoporous carbons are also a potential material for drug delivery [7] because show lower toxicity than mesoporous silica [8], and they are widely used for removing pesticides, metal ions, and organic pollutants, such as dyes, from textiles, paper, cosmetics, tanneries, and others industrial effluents [9-14].

Several synthesis method approaches have been described to develop carbon materials with well-designed morphology and tunable hierarchical pore size distribution according to its potential use [15-18]. The use of hierarchical carbon with a combination of tunable pore size can overcome some drawbacks, such as long diffusion pathways, slow ion transport, or pore-clogging, even produces a synergetic effect [19-22].

In general, the routes for obtaining the hierarchical carbon materials are based on a dual pore forming procedure, involving activation method (chemical or physical), and the use of a combination of hard and/or soft-templates as well as stabilizing agents [15]. These activation methods are mainly used to the formation of micropores in carbon materials [23,24]. Soft templates are organic molecules, which are able to form organized systems, such as vesicles, micelles or liquid crystals [25], and their use as templates typically

produces mesopores smaller than 20 nm. Also, Bruno *et al*. reported the use of cationic polyelectrolyte as a stabilizing agent for mesoporous carbon formation that, depending on the synthesis condition, produces mesopores of different sizes [26-28]. These porous forming agents are completely removed from the carbonaceous material during the carbonization step, avoiding the template removal in a subsequent step. However, these carbon materials have not a rigid structure, and their final structure can be affected by several variables (temperature, pH, ionic strength).

Inorganic templates, such as porous silica or aluminosilicate, offer a predictable porosity and structure. Knox *et al*. [29] pioneered the use of silica templates for the synthesis of porous carbon materials by polymerization of a phenol–hexamine mixture within the pores of silica gel, followed by pyrolysis of the resulting resin in a nitrogen atmosphere and dissolution of the silica template. Ryoo *et al*. [30] paved the road for a number of synthesis procedures using different silica ordered templates, like MCM-48 (Ia3d), SBA-15 (p6mm), SAB-16 (Im3m), KIT-6 (Ia3d), and FDU-1 (fcc), and several carbon precursors [31-33]. By using these methods, several carbon structures with a wide pore size distribution (even larger than 50 nm) have been reported [34]. Therefore, the use of low cost silica as a hard template, along with is relatively easy removal, allows the fabrication of structured carbon of practical interest without a severe impact on the production costs [35].

Although several methods to obtain hierarchical carbon were proposed, few reports deal with the preparation of carbon powder with bimodal mesopore size distribution, particularly those having pores below 10 nm and larger than 20 nm [36-38]. Carbons having that range of bimodal pore distribution could offer a large surface area, completely accessible to liquids in electrochemical systems, and improved characteristics for biomedical applications and waste treatment. In consequence, our goal is to fabricate porous carbon

powder with a balanced pore size distribution which includes macropores, mesopores and micropores obtained by using commercially available low cost pore-forming agents.

This work describes a novel strategy for the synthesis of hierarchical hard carbon material from structured resorcinol-formaldehyde, which was obtained by a combination of stabilizing agent (cationic polyelectrolyte) and a hard template (porous silica). One of the main advantages of this method for obtaining a carbon with bimodal hierarchical mesoporosity is its simplicity, as compared to other reported techniques. Also, this route provides a possible large scale production of hierarchical carbon material with a commercially available low cost hard template. Different mass ratios of polyelectrolyte and hard template were used in order to evaluate its effect on the pore size distribution, and we have analyzed the performance of carbons with different pore distribution sizes in relation to its capacity to adsorb methylene blue, which is widely used in textile, cosmetic, and paper industries.

2. EXPERIMENTAL PART

2.1. PREPARATION OF THE MESOPOROUS CARBONS

Hierarchical mesoporous carbons were obtained using resorcinol-formaldehyde (RF) resin as carbon precursors, sodium acetate as a catalyst, and a combination of structuring agent (SA), and a hard template (HT) as pore-forming agents. The structuring agent was poly(diallyldimethylammonium chloride), (pDADMAC, 20% in H_2O, average M_w= 100,000–200,000 $g \cdot mol^{-1}$, Sigma–Aldrich), while a commercial silica porous powder particle (Sipernat 50®, EVONIK) was employed as hard template. Moreover, glycerol and methanol were added to the aqueous media as a dispersant and wetting agents, respectively.

Figure 1 shows a scheme summarizing the different steps employed for the carbon synthesis procedure.

Briefly, two solutions called solutions A and B, were prepared (see the detailed compositions of both solutions in Table S1 of Supplementary Information).

Solution A contains resorcinol (R), sodium acetate (C), and pDADMAC dissolved in water. In solution B, Sipernat® 50 was completely dispersed in a mixture of water (W), methanol (M), and glycerol (G), by sonication during 15 min. Both solutions were mixed slowly by continuous stirring, and then heated at ebullition under reflux conditions. The pH of the mixed solution before heating was about 6.15. Polymerization starts by adding formaldehyde, which it was carried out in two steps. The first aliquot was added 20 minutes after that the mixed solution reached the boiling temperature. After 45 minutes the second formaldehyde aliquot was added, and the reaction temperature was maintained for 90 minutes. Then, the reaction mixture was cooled and a light pink precipitate was separated from the reaction media by filtration under vacuum. The supernatant was clear, indicating that almost all the silica particles were contained in the precipitate. The solid obtained was dried at 80 °C in vacuum for 24 h.

All the synthesis were performed employing the following constants weight ratios of the reactants R/F=1.15, R/C=8.30, R/W=0.0215, R/G=0.29, and R/M=0.50, while the pDADMAC and/or the silica amounts were varied. The dry resin-silica composite obtained was heated in a tubular furnace under nitrogen stream at a heating rate of 3 $^{o}C \cdot min^{-1}$, and complete carbonization of the sample was achieved by holding the temperature of the furnace at 1000 ^{o}C for 120 min. In order to remove the hard template the carbonized sample was washed in 3 M NaOH at 60 °C, in a reflux system for 24 h. Then, the powder was washed with deionized water in a Soxhlet apparatus until reaching a neutral pH (*ca*. 12 h).

Finally, the resulting mesoporous carbon was dried at 80 °C and kept in closed vessels for further characterizations. The samples were identified as P_xS_y, indicating the amount "x" of polyelectrolyte (P) and the amount "y" of silica (S) used to prepare the carbon precursor. Thus, a sample containing 0.4 g of pDADMAC and 1.0 g of silica is denominated $P_{04}S_{10}$ (see Table S1 in Supplementary Information). The series "$P_{04}S_y$" corresponds to samples having the same amount of pDADMAC (0.4 g) and a variable amount (y) of silica.

2.2. CHARACTERIZATION OF THE MESOPOROUS CARBONS

An ASAP 2020 (Micrometrics) instrument was used to determine the nitrogen adsorption-desorption isotherms at -196 ºC. The Brunauer-Emmett-Teller (BET) equation was used for determining the specific surface area [39]. The total volume was calculated at relative pressure, $p/p^0 = 0.99$. The pore size distribution (PSD) was determined from the desorption branch by using the Barrett–Joyner–Halenda (BJH) model [40], whereas the same model was used for the mesopore volume determination from the adsorption branch. The micropore volume (pores size < 2 nm) was calculated using the t-plot method [41].

Scanning Electronic Microscopy (SEM) of the carbon samples were carried out in a Carl Zeiss NTS-SUPRA 40 operated at 5kV. Thermogravimetric analysis was carried out with a DTG-50 (Shimadzu) simultaneous DTA-TG thermal analysis system. The samples were located in an alumina cell, and the scan was performed from 25°C up to 1000 °C at a heating rate of 10 °C·min^{-1} under air flow (40 cm^3·min^{-1}).

The particle size distribution of the carbon powder was determined by laser diffraction (Mastersizer 2000S, Malvern) using water as a dispersion medium (stirring at 1750 rpm).

Raman spectra were recorded with a LabRAM HR Raman system (Horiba Jobin Yvon), equipped with two monochromator gratings and a charge coupled device detector. The

scattered light was collected with a spectral resolution of 1.5 cm^{-1}. Argon laser line at 514.5 nm was used as an excitation source. The measurements were performed in a backscattering geometry, with a 50x magnification. The *pseudo*-Voigt functions were chosen for the fitting of the experimental data [42].

The determination of the surface concentration of functional group was carry out following the procedure described by Boehm [43], taking into account the experimental observations proposed by Andreas and coworkers [44,45]. For a typical titration, a known mass of carbon (~ 400 mg) was added to 10 cm^3 of one of three 0.05 M reaction bases $NaHCO_3$ (Baker Analyzed, 99.7%), Na_2CO_3 (Carlo Erba Reagents, 99.5%) and NaOH (Carlo Erba Reagents, 99%). The samples were stirred for 24 hrs and then filtered to remove carbon. Aliquots of the remaining solution were acidified with standardized 0.05M HCl and then back-titrated with standardized 0.05 M NaOH. Titration endpoints were determined potentiometrically using a HANNA HI 221 pH meter. In all cases, the solutions were prepared with fresh milliQ water (18.2 MΩ) and CO_2 was removed from solution by N_2 bubbling immediately before the titration. Blank experiments containing no carbon were also performed for each reaction base.

Zeta potential measurements were performed with a Zetasizer 2000 instrument (Malvern Instruments). Carbon sample $P_{04}S_{10}$ was appropriately dispersed in aqueous solution at different pH values, adjusted by adding HCl or NaOH to the aqueous dispersions. The final pH values were measured using a pH-meter (HI 3222, Hanna Instruments). The dispersion ionic strength was fixed at 1.0 mM using KCl and 10 mM LiCl. All suspensions were equilibrated at least 30 minutes in order to obtain stable pH and zeta potential readings.

Powder X-Ray Diffraction (PXRD) patterns were collected in a Siemens D5000 diffractometer, employing Cu kα source operating at 40 kV and 30 mA. The angle extended

from 20 to 100º with a 0.05 degree step size and four seconds time step. The in-plane graphitic crystallite size (*La*) and the crystallite size along the c-axis (*Lc*, stacking size) were computed using the Scherrer equation [46] from the full-width-at-the-half-maximum (FWHM) of the (100) and (002) Bragg peaks, respectively. The inter-graphene layer spacing (d_{002}) was determined from the position of the maximum of the (002) Bragg peak with the assistance of the Bragg equation.

Small angle X-Ray scattering (SAXS) was performed with a XEUSS 1.0 (XENOCS) equipment with a Pilatus100K (DECTRIS, Switzerland) X-Ray detector with a Cu Kα 1,2 (λ= 1.54178 Å) source and a sample-detector distance of 1334,94 mm. The SAXS pattern was recorded as a function of the modulus of the scattering vector, defined as,

$$q = \frac{4\pi sen\,\theta}{\lambda} \quad (1)$$

where θ is half of the scattering angle. Each SAXS pattern corresponds to an average of three set data collected during 120 seconds per each, with a *q*-range from 0.0005 - 0.27 $Å^{-1}$ (2θ ranges from 0.007º to 3.789º).

2.3 METHYLENE BLUE ADSORPTION ONTO MESOPOROUS CARBONS

Analytical grade methylene blue (MB, Merck Co.) was dissolved in deionized water (18 MΩ·cm resistivity) for the preparation of a 0.5 $g \cdot dm^{-3}$ MB stock solution. All solutions used were prepared by the dilution of the stock solution.

For the adsorption kinetic studies, 50 mg of carbon powder (particle size between 10 and 100 µm, see Figure S4, SI) was added to 100 cm^3 of a solution containing 50 $mg \cdot dm^{-3}$ of MB, under continuous stirring. Aliquots of 1 cm^3 were taken at different times, and

immediately centrifuged to minimize the interference of the remaining carbon particles with the analysis.

For the adsorption equilibrium experiments, 5 mg of carbon powder was added to 25 cm^3 flasks with 20 cm^3 of MB solution of different concentrations (50, 75, 100, 150, 200, 250, 350 and 500 $mg \cdot dm^{-3}$). The flasks were left under stirring for at least 72 h. In order to ensure equilibrium conditions. Upon equilibration the carbon powder was separated by centrifugation. In all cases, the concentration of MB in the solutions was determined by UV-VIS spectroscopy (Ocean Optics Red Tide USB650). The MB adsorption capacity of the carbon at each time, q_t, was calculated as:

$$q_t = \frac{(C_o - C_t) \cdot V}{W} \quad (2)$$

where c_o is the MB initial concentration, c_t is the MB concentration at time t, V is the volume of solution, and w is the mass of the mesoporous carbon sample.

Infrared spectra of the carbon before and after the MB adsorption were recorded with an Avatar 320 FT-IR (Thermo Nicolet), between 4000 and 500 cm^{-1}, averaging 32 scans. Pellets were prepared by mixing 1 mg of the carbon sample with 500 mg of KBr (Merck, spectroscopy grade).

For evaluating the effect of pH on carbon adsorption capability, 100 mg of the $P_{04}S_{10}$ carbon powder was added to three different flasks with 30 cm^3 of 350 $mg.dm^{-3}$ MB solutions at pH 2.0, 4.5, and 6.1, respectively. The samples were stirred until equilibrium conditions were achieved (> 72 h.), and then the maximum adsorption capacity (MAC) of the carbon powder was determined at each pH as it was described previously.

3. RESULTS AND DISCUSSION

3.1. CHARACTERIZATION OF THE HARD TEMPLATE

Adsorption-desorption isotherms and pore size distribution (BJH model, desorption branch) of the commercial silica particles used as hard template are shown in Figure 2. Sipernat 50® is formed by sponge-like silica particles as shown in Figure S1 (Supplementary Information). According to the supplier [47], the tapped density is 0.175 $g \cdot cm^{-3}$ and, considering that in a close packing of spheres the interstitial volume is 26%, the apparent density of the silica spheres is 0.236 $g \cdot cm^{-3}$. This would indicate that only *ca.* 10% of the particle´s volume is mass of silica (silica density, 2.2 $g \cdot cm^{-3}$). The particle size distribution (Figure S3 Supplementary Information) extends in the range 2 - 250 μm, with an intense peak ca. 70 μm and a smaller shoulder around 15 μm. The calculated BET surface area was 475 $m^2 \cdot g^{-1}$, and a broad PSD with a maximum around of 20 nm was obtained for commercial silica powder (Fig. 2). The mesopore volume was 1.10 $cm^3 \cdot g^{-1}$, while the micropore volume is negligible. Thus, the silica template has a large free space without micropores contribution, and *ca*. 75% of volume corresponds to pores larger than 50 nm, which would be completely accessible to liquids. Moreover, the outer surface of the silica particle is negligible respect to the inner porous surface.

3.2. EFFECT OF THE PORE FORMING CONTENT ON PORE SIZE DISTRIBUTION OF THE MESOPOROUS CARBONS.

The effect of pore forming agents on the PSD was analyzed as a function of two synthesis parameters: the pore volume on silica (V_S), and the volume of RF resin (V_R). The ratio

(V_R/V_S) determines the fraction of resin that can penetrate into the pores of the hard template.

An approximate density of the RF resin was obtained from monolithic RF pieces synthetized in absence of silica. In this case, the polymerization conditions were slightly modified in order to produce monolithic RF, and the apparent density was calculated from the volume and weight for each piece. The pore volume of silica was calculated from the mass of silica used in the synthesis, and the porosity and apparent density of the silica spheres. Details of the calculation of V_R and V_S are given in Supplementary Information, while in Table 1 are summarized the values of these parameters for each all samples synthesized.

The particle size distribution and the maxima particle size of the carbon powders are shown in Figure S4 and Table S2 (Supplementary Information), respectively. The particle size range for the series $P_{04}Sy$ was between 10 and 50 μm. The particles distribution showed no trend respect to silica content in the polymerization media. On the other hand, the sample $P_{00}S_{20}$, pDADMAC-free, showed a maximum around 105 μm.

Figure 3a shows the nitrogen adsorption-desorption isotherms for carbons from $P_{04}S_{01}$ to $P_{04}S_{60}$ ("$P_{04}S_y$" series) which were obtained by using both, pDADMAC and silica, as pore forming agents. Also shown are $P_{04}S_{00}$ and $P_{00}S_{20}$ samples, which correspond to carbons obtained without the use of silica and pDADMAC, respectively. The corresponding pore size distribution (PSD), obtained by using the BJH model from the desorption branch, is shown in Figure 3b. In order to analyze the evolution of the pore formation in the samples, the mesopore volume (from BJH, adsorption branch) was arbitrarily separated in pores below 10 nm ("small pores"), and above 10 nm ("large pores"), as shown in Figure 3c.

The porous carbons obtained by using only silica ($P_{00}S_{20}$) or only pDADMAC ($P_{04}S_{00}$) as

pore-forming agent show a type IV isotherm with a hysteresis loop H1, according to IUPAC classification [48], which is characteristic of materials formed by particle agglomerates, or packed uniform spheres, with a rather narrow PSD. Thus, these carbons, prepared with a unique pore-forming agent, show a narrow monomodal PSD, with peaks around 9 nm and 16 nm for the samples $P_{00}S_{20}$ and $P_{04}S_{00}$, respectively.

The monomodal PSD persist in samples with low silica content, such as $P_{04}S_{01}$ and $P_{04}S_{02}$, and the peak of the PSD shifts from 16 to 25 nm (see Fig. 3b). In these samples the volume of "small pores" is low, while the volume of "large pores" tends to increase with increasing silica content, as shown in Figure 3c. A strong decrease of the volume of "large pores" is observed for sample $P_{04}S_{05}$ and, at the same time, a small peak around 5 nm is observed in the PSD.

In samples with higher silica content ($P_{04}S_{10}$ to $P_{04}S_{60}$), a gradual appearance of two hysteresis loops in the adsorption-desorption isotherms, depicted in Fig. 3a, can be appreciated, which is indicative of well-developed bimodal mesopores networks. For these samples of the "$P_{04}S_y$" series the "small pores" size remains at 5 nm by changing the silica content, although its contribution to the pore volume increase with increasing silica content. On the other hand, the "large pores" size distribution becomes broader and larger, and its contribution to the pore volume tends to decrease with increasing silica content, as indicated in Fig. 3c.

It is worthy to compare the pore volume results for "$P_{04}S_y$" series to those obtained for sample $P_{00}S_{20}$ (without pDADMAC), as shown in Fig. 3c. The total mesopore volume in "$P_{04}S_y$" series shows a gradual increasing trend with increasing silica content, mainly due to the contribution of "small pores". The total pore volume of the $P_{04}S_{20}$ sample is more than twice the total volume of the sample $P_{00}S_{20}$, having the same amount of silica but without

stabilizing agent, indicating a synergetic effect when both pore-forming agents are used.

In summary, the results obtained for "$P_{04}S_y$" series seems to indicate the preferential formation of mesopores smaller than 10 nm as the mass fraction of silica in the carbon precursor composite increases.

In order to corroborate that the small pores of 5 nm are formed by using silica as hard template, N_2 adsorption isotherms of the sample $P_{04}S_{30}$, before and after silica removal, were performed. The results are depicted in Figure 4. The PSD of the $P_{04}S_{30}$ sample before removing the silica shows a broad band around 30 nm that can only be originated by the pDADMAC. After silica removal from the sample a pronounced peak around 5 nm was observed, while the broad band becomes slightly more intense, and it seems to shift toward smaller sizeshydrox.

In view of this result, we conclude that the pores around 5 nm are formed by dissolution of the hard template, but also the silica elimination contributes to the formation of the larger pores with a slight modification of the amount of mesoporosity in the region of 10-50 nm.

The structures of the prepared carbons were analyzed by SEM, and the images of samples $P_{04}S_{00}$, $P_{00}S_{20}$, and $P_{04}S_{30}$ are shown in Fig. 5 (a-c). Sample $P_{04}S_{00}$ (only pDADMAC pore forming) shows a poorly packaged sponge-like structure, formed by globular shape carbon particles, *ca*. 10 nm in size, like the region marked with a circle. This sample has an open structure with maximum pore size distribution around 16 nm (determined by N_2 adsorption, as shown in Figure 3b). Sample $P_{00}S_{20}$ (only silica as pore forming) shows a more compact globular structure than sample $P_{04}S_{00}$, like region marked with a dashed circle. Although the pores size cannot be well appreciated in the SEM image, N_2 adsorption results (Fig. 3b) indicates that pore sizes are in the range 7-12 nm.

In the case of the $P_{04}S_{30}$ sample, Fig. 5c, a hierarchical structure originated by both pore

forming agents is observed. The micrograph shows the presence of regions formed by interconnected carbon nanoparticles, like those marked with a circle, similar to sample $P_{04}S_{00}$ (Fig. 5a). However, there are other regions (marked with dashed circles) showing clusters of carbon nanoparticles with a more closed packing, similar to sample $P_{00}S_{20}$ (Fig. 5b).

How can we explain the peak close to 5 nm found in the samples prepared with silica as hard template?. As mentioned in Section 3.1, Sipernat® 50 is a sponge-like structure formed by the aggregation of silica nanoparticles with globular shape around 6 nm in diameter, which would originate pores close to this size by replication. The "large pores" (> 10 nm) should be then promoted by the presence of pDADMAC in the resin/silica composite. It has been demonstrated that cationic polyelectrolyte, like pDADMAC, adsorbs on the surface of the polymer (RF) nanoparticles stabilizing and structuring them, avoiding the collapse of the RF resin porous structure during the drying and leading to the formation of mesopores in the carbons [26,49]. In our synthesis procedure, pDADMAC also adsorbs [50] on the negatively charged silica surface [51] generated at the initial pH (6.15) of the polymerization media. This hypothesis was confirmed using a dispersion of silica and pDADMAC with a mass ratio similar to that of sample $P_{04}S_{30}$, showing that *ca*. 86% of pDADMAC was sorbed into the silica (see section 4 in Supplementary Information). However, the degree of penetration of pDADMAC inside of the silica pores could not be determined in the synthesis procedure employed. The radius of gyration for pDADMAC with average M_w = 100,000–200,000 $g \cdot mol^{-1}$ was reported to be around 20 to 40 nm in solution [52,53]. Although electrostatic driving force promotes the penetration of the polyelectrolyte into the pores, the adsorbed conformation and space occupied by the pDADMAC inside the pore is not known under the polymerization conditions. Thus, we

expect that only a fraction of the total pore volume of silica would be accessible to pDADMAC. Therefore, the structuration of the RF resin by pDADMAC in the presence of porous silica is complex to elucidate, but it is clear that pDADMAC outside and inside the silica mesopores is responsible for the formation of pores larger than 10 nm.

Moreover, the pDADMAC and silica elimination from the carbon originate macropores undetected by N_2 adsorption technique, but visible in the SEM images depicted in Figure S2 (Supplementary Information).

In order to determine the carbon chemical stability, the samples $P_{04}S_{00}$, $P_{00}S_{20}$, and $P_{04}S_{30}$ were analyzed by thermogravimetry under an air stream. As shown in Figure S5 (Supplementary Information), all the samples loss between 5 % and 10 % w/w of water when heated up to 100 ºC, and exhibit an excellent thermal stability up to temperatures close to 500 ºC (samples $P_{04}S_{00}$, $P_{00}S_{20}$) and 400 ºC (sample $P_{04}S_{30}$). The decreases of the oxidation temperature for $P_{04}S_{30}$ sample could be due to its more open structure. The most expected applications of these mesoporous carbons are: removal of water pollutans, catalysts support in PEM fuel cells, cathodes of lithium-air batteries, and electrodes of supercapacitors. Taking into account that all the mentioned systems work at moderate temperatures (< 150 ºC), the thermal stability for the analyzed samples can be considered as quite acceptable.

3.3. SURFACE AREA AND PORE VOLUME CHARACTERIZATION

Figures 6a and 6b show the surface area (BET), the micropore surface area (t-plot), the total pore volume (measured at p/p^o = 0.99) and the micropore volume *vs*. the mass fraction of the pore forming agents, defined as $f_{PFA}= (m_{SA}+m_{HT})/(m_{HT}+m_{SA}+m_{RF})$, for all carbon samples synthetized. In addition, the values obtained are given in Table S3 of the

Supplementary Information.

The carbons obtained by using a single molding agent (samples $P_{00}S_{20}$ and $P_{04}S_{00}$) have a total surface area and micropore surface around 700 and 400 $m^2 \cdot g^{-1}$, respectively, while their total pore volume is around 0.7 $cm^3 \cdot g^{-1}$. Porous carbon obtained by using pDADMAC as pore formation agent (sample $P_{04}S_{00}$) has a similar surface area than those previously reported [4,8], while there is a lack of information for carbon materials obtained from silica as hard template (sample $P_{00}S_{20}$). In general, a high surface area with low contribution of micropores and large pore volume were obtained for all the samples, by increasing the amount of the pore forming agents. This result could be attributed to the development of "small pores", as discussed in section 3.2, which make a larger contribution to the surface area than the "large pores".

For the "$P_{04}S_y$" series, the surface area tends to increase as the mass fraction of silica increases, from *ca*. 700 $m^2 \cdot g^{-1}$ for the sample $P_{04}S_{00}$ up to *ca*. 1000 $m^2 \cdot g^{-1}$ for the sample $P_{04}S_{30}$. Moreover, a decreasing trend in the micropore surface area can be observed as f_{PFA} increases. Thus, when f_{PFA} increases for each pore forming agent, SA or silica separately, the ratio S_{mic}/S_{BET} decreases from 0.6 down to 0.2. In Figure 6b, the trend of the total pore volume increases with the fraction of the pore forming agents, reaching 1.7 $cm^3 \cdot g^{-1}$ for the sample $P_{04}S_{30,}$ while the micropore volume showed a decreasing trend as f_{PFA} increases.

The carbons synthetized with low f_{PFA} showed a high micropore volume (around 0.13-0.15 $cm^3 \cdot g^{-1}$), that decreases (down to 0.04 $cm^3 \cdot g^{-1}$) as the f_{PFA} fraction increases, while V_{mic}/V_{total} ratio decreases from 0.17 down to, an almost negligible, 0.02. In comparison, carbons xerogels obtained by similar procedures (sol-gel synthesis and dried in an air convection oven), showed a comparable V_{mic}/V_{total} ratio, around 0.15 [54]. In the case of monolith mesoporous carbon obtained by using only pDADMAC [28] or F127 [55] as

structuring agent, the V_{mic}/V_{total} ratios are 0.10 and 0.24, respectively. Moreover, the PSD profile in the micropore region exhibits a peak at 1.1 nm that does not shift with changes in f_{PFA}, or with the pore forming agent used in the synthesis (see Fig S6 in Supplementary Information).

This result is an important feature in the synthesis of hierarchical carbon materials for certain applications. Thus, high surface areas with low micropore content in carbons used as catalytic support (involving a liquid phase) offer not only a better catalyst dispersion, but also a higher catalytic activity [56].

3.4. SURFACE CHEMISTRY

In order to determine the surface charge density of the carbon materials and the chemical nature of the surface functional groups, Boehm titration [43] was carried out on the samples $P_{04}S_{00}$, $P_{04}S_{30}$, and $P_{00}S_{20}$. Bases of various strengths ($NaHCO_3$, Na_2CO_3 or NaOH) neutralize different surface groups (carboxylic, lactonic, and phenolic), and the surface concentration of each group can be determined by the difference between the uptake of each base [44,45].

The specific and surface concentrations of the three functional groups analyzed are summarized in Table 2. If the group specific concentration ($\mu mol \cdot g^{-1}$) of functional groups is normalized by the BET surface area of each carbon, the group surface concentration ($\mu mol \cdot m^{-2}$) is obtained. It is observed that no significant differences for the group surface concentrations are observed among the samples.

The carbons present a majority of phenolic functional groups (≈ 55%) due to the fact that the carbons were prepared with the same amount of resorcinol-formaldehyde resin and,

consequently, the phenolic group remains in the carbon matrix after carbonization at 1000ºC. A lower amount of carboxylic (≈ 35%) and lactonic groups (≈ 10%) was found in all the samples, in line with previously reported values for carbons prepared from resorcinol [57]. As results in Table 2 reveal, our carbon samples exhibits a total surface concentration of functional groups of 0.29 ± 0.021 μmol·m^{-2}, in good agreement with reported values for similar carbon materials [57]. This surface concentration is equivalent to approximately one functional group each 5 nm^2 that, in case of being ionized, would make a moderate contribution to the charge density.

The results of the zeta potential, ζ, measurement performed on the sample $P_{04}S_{10}$ are shown in Figure S7 of Supplementary Information. It is observed that the isoelectric point for the carbon particles correspond to pHs in the range 3.1-3.8, depending on the electrolyte, which is a value close to that found for mesoporous carbons having a larger amount of carboxylic (pKa ≈ 4-5) and phenolic (pKa ≈ 10) groups in comparison to carbonyl groups (pKa ≈ 16-20) [58]. By employing the following equation, valid for $1 < \kappa a < 200$, [59]

$$\sigma_\zeta = \varepsilon \frac{kT}{ze} \kappa \left[2 \sinh\left(\frac{z\zeta}{2}\right) + \frac{4}{\kappa a} \tanh\left(\frac{z\zeta}{4}\right) \right] \qquad (3)$$

where κ is the reciprocal of the Debye distance (≈ 1.04 nm^{-1} in KCl 1 mM), a is the particle size (≈ 100 nm), z is the ion charge, ε is the media permittivity, we estimated from the zeta potential in KCl 1 mM (≈ -30 mV) a surface charge density σ_ζ ≈ 0.24 μmol·m^{-2}, in very good agreement with the titration result.

3.5. RAMAN SPECTROSCOPY AND X-RAY DIFFRACTION ANALYSIS

In order to elucidate the microstructure of the obtained hard carbons, samples $P_{04}S_{00}$,

$P_{04}S_{01}$, $P_{04}S_{05}$, $P_{04}S_{15}$, and $P_{04}S_{30}$ were analyzed by Raman spectroscopy. Figure 7 shows the Raman spectra of the carbon samples, along with the corresponding spectra deconvolution, whose parameters are summarized in Table 3.

All samples exhibit the typical broad D and G bands, characteristic of highly disordered carbons [60-63]. Ferrari and Robertson showed that G mode has a E_{2g} symmetry and is originated by the vibration of the in-plane bond-stretching of the sp^2 C of the hexagonal graphene sheets [64]. For the analyzed samples, this band appears at the typical region corresponding to the graphitic carbons (~1600 cm^{-1}) [65]. The D band around 1350 cm^{-1} is forbidden in perfect graphite and becomes active in the presence of disordered graphene structures According to Li *et al*. [63], two additional bands (M1 and M2) are needed to properly fit the Raman spectra of hard carbons. In addition, it is well established that the relation between the intensities of the D and G bands – I_D/I_G or $I_D/(I_{D+}I_G)$ – are correlated with the degree of structural disorder of the hard carbon [65]. The I_D/I_G and $I_D/(I_{D+}I_G)$ ratios do not show any significant dependence on the synthesis conditions, revealing that all the synthesized materials are hard carbons with the same degree of structural disorder (Table 3).

In order to get a deeper insight on the carbon microstructure, the XRD patterns of the same samples were determined. Figure 8 shows that all samples present broad peaks around 23º and 43º, identified as the (002) and (100) diffraction of graphitic layers, typical of highly disordered carbons [66,67].

The interlayer graphene spacing (d_{002}) decrease from 0.392 nm to 0.376 nm, with decreasing V_R/V_S (see Table 4). It is worth to note that these results show an expansion of the graphene inter-layer distance with respect to graphite (d_{002} = 0.335 nm) [67], being these materials possible candidates for electrochemical intercalation, not only of lithium,

but also of sodium [4,6]. The intercalation properties of these materials are currently under study and are outside of the scope of the present work.

In order to characterize the parallel stacking of graphene, Dahn and coworkers [66.67] introduced the empirical parameter *R*, defined as the ratio between the total to the background intensity at the (002) Bragg peak position. $R = 1$ for an ideal hard carbon material composed only of single-layer micro-structures, and it increases as the fraction of single-layer micro-structures decreases. Table 4 shows that all the samples exhibit similar values for this empirical parameter, with an average $R = 1.83 \pm 0.11$.

According to Dahn and coworkers [66,67], this value was found for materials containing roughly 40% of single graphene layer. Thus, even though the ratio between silica and the RF resin changed, the total fraction of single graphene layers in the final carbon material is practically the same. Similar results were obtained by the analysis of the stacking size value (*L*c), which reflects the crystallite size along the c-axis, and is closely related to the number of stacked graphene sheets in the "c" direction. Table 4 reveals that as V_R/V_S decreases, the value of *L*c barely changes.

In order to estimate the average amount of stacked graphene layers of the analyzed samples the empirical amount Lc/d_{002} was calculated. As Table 4 shows, the average value for all the samples is 2.6 ± 0.3 nm, confirming the picture depicted above. Also, the lateral extent of the graphene sheets (*L*a), also known as "in-plane graphite crystallite size", was calculated from the (100) Bragg peak showing similar values for all the samples, with an average value of 3.40 ± 0.26 nm.

The SAXS pattern obtained for the samples $P_{04}S_{00}$ (pore size ≈ 15 nm), $P_{04}S_{60}$ (pore sizes ≈ 5 and 20-40 nm), and $P_{00}S_{20}$ (pore size ≈ 5 nm), as a function of the scattering vector, are

shown in Figure 9. The X-ray scattering is due to differences in the electronic density between the voids (pores) and the carbon aggregates in the matrix. The scattering intensity decay monotonously in the whole q-interval, indicating a random distribution of the scattering, similar to that observed in other amorphous carbons [68,69].

By using the Guinier approximation that relates the scattering pattern to the radius of gyration of the scatter centre, R_g, valid for $qR_g < 1.2$,

$$\ln I(q) = -\frac{R_g^2}{3} q^2 + \ln I_0 \quad (4)$$

we obtained for R_g the values 8.9 nm, 11.2 nm, and 6.7 nm for samples $P_{04}S_{00}$, $P_{04}S_{60}$, and $P_{00}S_{20}$, respectively. Considering that these are effective values which correspond to average of a particle size distribution, it is plausible to assign these dimensions to the carbon particles.

3.6. DYE ADSORPTION CAPACITY OF THE MESOPOROUS CARBONS

Samples $P_{04}S_{00}$, $P_{04}S_{02}$, $P_{04}S_{30}$, $P_{04}S_{60}$, and $P_{00}S_{20}$ were chosen for the methylene blue adsorption analysis, covering a wide range of BET's surface area (from 662 $m^2 \cdot g^{-1}$ up to 998 $m^2 \cdot g^{-1}$) and total pore volume (from 0.70 $cm^3 \cdot g^{-1}$ up to 2.10 $cm^3 \cdot g^{-1}$). Figure 10 shows the MB adsorption isotherms for samples $P_{04}S_{02}$ and $P_{04}S_{60}$ and the fits using the Langmuir adsorption model:

$$q_e = q_m K_L c_0 (1 + K_L c_0)^{-1} \quad (5)$$

where c_o is the equilibrium concentration of MB in the solution, q_e is the equilibrium adsorption capacity, q_m is the maximum monolayer adsorption capacity, and K_L is the

Langmuir constant. Also shown in Figure 10 are the isotherm fits using the Freundlich model, corresponding to the expression:

$$q_e = K_F c_0^{1/n} \quad (6)$$

where K_F is the Freundlich constant, and n is the heterogeneity factor, related to the adsorption intensity of the adsorbent.

The parameters for both models are summarized in Table 5. As it can be seen, the Langmuir model yields the best fit, and the maximum adsorption capacities (MAC) of MB derived from that model are 319 $mg \cdot g^{-1}$ for sample $P_{04}S_{02}$, and 431 $mg \cdot g^{-1}$ for sample $P_{04}S_{60}$.

In order to compare the surface areas reported for these carbons (Table S3 in Supplementary Information) with those calculated from the MAC, we have to adopt a reliable value for the area occupied by an adsorbed MB molecule. This parameter has been reported in the literature and varies from 1.03 nm^2/molecule [70] up to 1.3 nm^2/molecule [71]. In our calculation we used the value 1.2 nm^2/molecule [72,73], yielding surface areas of (721 ± 16) $m^2 \cdot g^{-1}$ for the sample $P_{04}S_{02}$, and (974 ± 20) $m^2 \cdot g^{-1}$ for the sample $P_{04}S_{60}$, in good agreement with the BET areas (717 $m^2 \cdot g^{-1}$ and 950 $m^2 \cdot g^{-1}$, respectively). Thus, we conclude that MB is adsorbed not only in the carbon mesopores but also in the micropores, even in the case of sample $P_{04}S_{60}$, with a fraction of micropore surface higher than 60%.

In Table S4 of Supplementary Information we compare these results with those reported for several mesoporous and activated carbons, and other nanostructured carbons, such as graphene, nanotubes and nanosheets for which textural information (surface area, pore volume, pore size) have been measured.

It is observed that in the case of mesoporous carbons [73-80] the MAC of our mesoporous carbon is larger than many of them having similar or even larger surface area (MC1, MC2), including nitrogen-rich [77] and ordered mesoporous carbon (OMC) [78], and mesoporous carbon nitride (MCN) [80], all of them having smaller pore size. The fraction of carbon area covered with MB for these samples varies from low values (6-18%) for the bimodal sample MC2, having pores of 2 nm and 5.5-7.5 nm, up to values between 66 and 92% for monomodal samples MC1 with pores of 3.8 nm.

Exceptions to this behavior are the mesoporous carbon MC3 prepared with a MnO template [75], and the bimodal mesoporous carbon doped with Fe/Ni nanoparticles [79], having a bimodal or wide pore size distribution, with pore diameters close to that reported for samples $P_{04}S_{02}$ and $P_{04}S_{60}$. These mesoporous carbons exhibit larger MAC than ours, even those having lower surface area. However, it should be noted that the area covered with MB for carbons MC3 and FeNi/MC are a factor 2 or 3 times larger than the total surface area, which is a result quite unexpected.

If we have a look on the results of Table S4 for the activated carbons [81-87], all of them having pore diameter in the micropore range or in the lower mesopore range (2 to 4 nm), we observe that most of the carbons have lower MAC than our mesoporous carbons, even when their surface area is much larger. It is also clear that the MB coverage area is much lower than the total surface area, with the exception of samples AC5, however it is not described the way in which the authors obtained the pore diameters. Regarding graphene [88], nanotubes [89,90], and nanosheets [91], their MAC is lower than that of our mesoporous carbon, except for the porous carbon sheets embedded with Fe/Fe_3C nanoparticles, which exhibit also an anomalous MB coverage.

In summary, the observed trend in the behavior of the MAC for MB seems to indicate that carbons with high surface area due to micropores are not the best ones for high adsorption capacity. Probably, the carbon pore´s architecture largely determines the MAC and also the adsorption kinetics. Figure 11 shows a scheme of the silica hard template with the resin embedded inside (left panel). The hard template is a sponge-like structure formed by the aggregation of globular silica nanoparticles around 6 nm in diameter, which would originate pores close to this size by replication. After carbonization and silica dissolution the resulting carbon has large mesopores (> 10 nm) partially connected to the small mesopores (< 10 nm), both of then connected to the micropore structure indicated as small dots (right panel). MB molecules, with size 1.41x0.55x0.16 nm^3 [9], can diffuse rapidly through the large and small mesopores, and finally reached the micropores where they are adsorbed slowly. The graphical abstract shows a scaled representation of the MB monolayer coverage proposed for our samples.

The low coverage fraction of most of the activated carbons can be due to the fact that their area is mostly due to microporosity, and MB covers the regions closer to the particle surface hindering the adsorption on the deeper micropores. It has been suggested that the presence of mesopores larger than 3.5 nm is vital for the adsorption of MB because of the size of this dye [73]. This is partially true, because our samples have between 18 and 61 % of microporosity area which is available for adsorption. We conclude that microporosity can help to enhance the adsorption capacity, provided that micropores are connected to mesopores that allow the dye to get deep into the carbon structure.

FTIR spectra analysis was also performed to gain insights into the adsorption mechanism of MB on the mesoporous carbon. The sorption of MB on the $P_{04}S_{10}$ sample does not modify appreciably the FTIR spectra of pristine carbon, as can be seen in Figure S8 of

Supplementary information. The intensity of the broad band between 3200 and 3700 cm^{-1} seems to keep unchanged, suggesting that hydrogen bonding, which has been proposed as one of the possible mechanisms for the adsorption of MB on activated carbon [92], would not be important in this case. The peak at 670 cm^{-1} is not affected by MB adsorption, contrary to that observed for the case of adsorption on multiwalled carbon nanotubes [90], where this peak becomes broader and decreases its intensity. This would indicate that the π-π stacking mechanism, suggested as one of the operating for the adsorption on carbon nanotubes is not occurring in the carbons prepared in this work. The only appreciable change, albeit small, in the FTIR spectra of the carbon with adsorbed MB, is that the peaks in the region 1000-1100 cm^{-1}, corresponding to the axial deformation of vibrations of –C–O bonds in phenols becomes broader upon MB adsorption, which may by assigned [3] to electrostatic interactions of the MB cation with the negatively charged groups on the carbon surface.

3.7. DYE ADSORPTION STABILITY AND PH EFFECT

MB adsorption experiments were performed on the $P_{04}S_{10}$ carbon in the pH interval from 2.0 up to 6.1. The Maximum adsorption capacity at pH of 2.0, 4.5 and 6.1 was 305 ± 7, 298 ± 7 and 295 ± 7, respectively. These results show that there is no significant effect of the pH on the MAC of MB on the carbon. As it was discussed previously, the q_m values obtained for the $P_{04}S_{10}$ carbon at different pHs reveals that MB is adsorbed not only on the carbon mesopores but also on the micropores. Additionally, it can be concluded that even when MB (methylthioninium chloride) is an ionic dye, the methylthioninium cation is not adsorbed in major extension at higher pH, where the negative charge density should be

higher, because of the low surface concentration of ionizable groups, as discussed in Section 3.4.

In order to explore the MB adsorption stability, two carbon samples loaded with MB at their MAC were left in water at different pH (2.0 and 6.0), under stirring for 48 hours, at room temperature. Afterwards, the percentage of MB release to the water was 0.18% and 0.42% for pH 6.0 and 2.0, respectively. The larger retention of the ionic MB at pH 6.0 is probably due to the increases of the negative charge density on the pores surface with increasing pH, and confirms that the main mechanism of MB adsorption on the carbon is through electrostatic interaction. The observed adsorption stability is in line with the findings during the adsorption kinetics experiments, where MB (at a concentration below the MAC) was irreversibly adsorbed on the carbon samples at room temperature, leaving a clear water solution, even after several days of contact.

We also explored the effect of the temperature on the MB adsorption stability. The previous carbon samples, saturated with MB and equilibrated at pH 2.0 and 6.0, were heated up to 70 ºC and stirred again during 48 h. It was observed that, even at these extreme conditions, only 0.30% and 0.63% of the MB adsorbed was released to the water for the solutions at pH 6.0 and 2.0, respectively. Thus, these experiments show that our material exhibits an almost irreversible pollutants adsorption that could not be removed by pH or temperatures changes. The pollutant final disposal can be performed, for instance, by burning it along with the carbon.

3.8. DYE ADSORPTION KINETICS

Figure 12 illustrates the uptake of MB by 50 mg of mesoporous carbon samples from 100 cm^3 of solutions containing 50 $mg \cdot dm^{-3}$ of MB. It is observed that the removal of MB from

the solution is complete in less than 2 minutes for samples $P_{04}S_{30}$ and $P_{04}S_{60}$, it takes ≈ 30 minutes for sample $P_{00}S_{20}$, and more than 100 minutes for samples $P_{04}S_{00}$ and $P_{04}S_{02}$.

Usually, the kinetics of dyes onto activated carbons is described by resorting to three types of models, namely the pseudo-first-order model [93],

$$\ln (q_e - q_t) = \ln \ q_e - k_1 t \quad (7)$$

The pseudo-second-order model [94],

$$\frac{t}{q_t} = \frac{1}{k_2 q_e^2} + \frac{t}{q_e} \quad (8)$$

and the intra-particle diffusion model [95],

$$q_t = k t^{1/2} + C \quad (9)$$

where *k* is the corresponding rate constants.

The results summarized in Fig. 12 cannot be adjusted using the pseudo-first-order model, but they all obey the pseudo-second-order equation (8), with coefficients of determination higher than 0.999 (Table S5, Supplementary Information), in agreement with the conclusions of reported studies on the adsorption of MB on different types of adsorbent carbons [74,76-78,80,82,87-92].

The rate constants for the samples analyzed are reported in Table 6, along with the textural parameters and the average pore diameter of the monomodal and bimodal mesoporous carbons.

The rate constant for the adsorption of MB is much higher for the carbon samples $P_{04}S_{30}$ and $P_{04}S_{60}$ with bimodal pore size distribution that exhibits the highest surface area and pore volume due to mesoporous, that is, the lowest ratio A_{mic}/A_{tot} and V_{mic}/V_{tot}. The monomodal samples $P_{00}S_{20}$, $P_{04}S_{00}$, and $P_{04}S_{02}$, with a larger fraction of microporous area,

adsorb MB slowly. Even for these samples the process is almost complete within one hour, which is also comparable with the best reported adsorbent carbons, as can be seen in Table S5, where we compare the pseudo-second-order rate constant, k_2, with those reported in the literature [73-76,78-80,82,88-90,96-98].

These results reinforce the previous argument based on the MCM, that is, microporosity can help to enhance the adsorption capacity, provided that micropores are connected to mesopores, but bimodal mesoporous carbons with high mesoporous area display high MCM and fast adsorption kinetics.

By resorting to the intraparticle diffusion model (eqn. 9) it is possible to distinguish three kinetic regions characterized by different slopes, k, and intercept, C, as shown in Figure 13. It is observed that the intercept for the first and second linear regions follows the order $P_{04}S_{60} \approx P_{04}S_{30} > P_{04}S_{00} > P_{04}S_{02} \approx P_{00}S_{20}$. The value of C is supposed to be related to the diffusion resistance, given by the thickness of the boundary layer [87,99], which depends on the stirring intensity during the process.

The parameters of the intraparticle diffusion model for the studied samples are reported in Table 7. For sample $P_{04}S_{60}$, the first region occurs in less than one minute, so only constants k_2 and k_3 are reported.

Some studies of the adsorption kinetic of MB onto carbon nanotubes [89,90] and activated carbon [96] only analyzed the intermediate adsorption region, and reported a single k and C constants. Other authors analyzed the intermediate- and long-time kinetics [13,75,82] and reported two sets of constants, the large slope of the first linear region was attributed to the diffusion through the external boundary layer, while the small slope of the second (long-time) linear region was assigned to the intraparticle diffusion (which indeed correspond to

diffusion through the pores). However, the second slope is almost zero in these cases, and one should conclude that this second linear region corresponds to the equilibrium stage.

Three kinetics stages, as revealed by the intraparticle diffusion model for our mesoporous carbon, has also been found by Bedin *et al*. [87] for a microporous activated carbon (AC7 in Table S4). They assigned the three sequential kinetic to: i) the external diffusion of the adsorbate through the boundary layer from the adsorbent surface, (ii) diffusion through pore or intraparticle diffusion, and (iii) the adsorption of the adsorbate on the surface active sites.

We believe that the three regions in the case of our mesoporous carbons have a different interpretation. The first region with fast kinetic would represent the adsorption of MB on the external surface and macropores of the carbon particles, after diffusion through the boundary layer. The second region corresponds to the diffusion through the mesopores, while the slow final region is characterized by the diffusion of the adsorbate through the micropores.

4. CONCLUSIONS

Carbon powders with a bimodal mesopores size distribution have been successfully synthesized by a dual pore forming agent strategy, by resorting to a procedure that involves a fast synthesis step, a cationic polyelectrolyte as a stabilizing agent, and a low-cost commercial silica as hard template.

The observed bimodal mesopore size distribution was more sensitive to changes in the mass fraction of pDADMAC than that of silica. Carbon materials with pores around 6 nm have been formed by using commercial silica as hard template, while larger mesopores in the bimodal PSD, with diameters over the range from 12 to 40 nm, are attributed to the use

of a cationic polyelectrolyte, and to voids within the partially filled macropores of the silica hard template when $V_R/V_S < 1$.

The synthesized carbons have surfaces area in the range from 662 to 998 $m^2 \cdot g^{-1}$, and a pore volume from 0.70 to 1.70 $cm^3 \cdot g^{-1}$. Micropore contribution to the surface area decreases with increasing mass fraction of silica in the polymerization media. This result shows that the main contribution to increase the surface area is due to mesopore formation.

From the combination of the Raman spectroscopy and X-ray diffraction analysis, we conclude that, regardless the V_R/V_S ratio in our synthesis, all samples present a spatial distribution of no periodically ordered mesopores and a similar hard carbon microstructure. The synthesized materials have a disordered mesoporous structure, and contain roughly 40% of single-layer microstructures, an average of 2.6 stacked graphene layers with an interlayer separation around 20% higher than pristine graphite, and in-plane graphitic crystallite size around 3.4 nm. It is important to point out that our carbon synthesis scheme offers the flexibility to obtain materials with different surface area and different pore size distribution, while preserving the same hard carbon microstructure.

Bimodal mesoporous samples prepared with high silica content, which have the largest fraction of mesoporous area, exhibit the highest adsorption capacity and adsorption kinetic toward MB. The surface chemistry of the prepared carbons and the FTIR analysis seems to indicate that the main mechanism of MB adsorption on these carbons is the electrostatic interaction between the dye cation and the negative charge groups (predominantly phenolic) The MB adsorption is rather irreversible at the effect of pH and temperature (in the range 20-70 ^oC) on maximum adsorption capacities is small. On the basis of the degree of MB coverage we conclude that microporosity can help to enhance the adsorption capacity, provided that micropores are connected to mesopores that allow the dye to diffuse

deeper into the carbon structure.

This control on the properties of the material, along with their hard carbon microstructure, prompts our carbons as highly promising not only for pollutant removal from water but also in the field in the field of energy storage, as is the case of electrodes for lithium batteries. This particular application will be addressed in a forthcoming work.

5. ACKNOWLEDGMENTS

The authors thank financial support from Agencia Nacional de Promoción Científica y Tecnológica (ANPCyT) (PICT 2013-1818) and Consejo Nacional de Investigaciones Científicas y Tecnológicas (CONICET, PIP 112 201301 0808). They also thank the Departamento de Física de la Materia Condensada, Gerencia de Investigación y Aplicaciones (GIyA-CNEA) for the thermogravimetric analyzes, the Laboratorio I&D del PNGRR (Programa Nacional de Residuos Radiactivos) for the particle size analysis, Alejandro Wolosiuk (Gerencia de Química, CAC-CNEA) for the zeta potential measurements and interpretation, and Federico Movilla (INQUIMAE) for FTIR measurements. SAXS experiments were carried out in the X-Ray dispersion facilities of the Instituto de Investigaciones Fisicoquímicas Teóricas y Aplicadas (INIFTA-CONICET-UNLP). MMB, HRC, MJ, EdlL, and FAV are staff members of CONICET. EFQ thanks a Doctoral fellowship from CONICET.

6. REFERENCES

[1] A. Krüger, Carbon materials and nanotechnology, Wiley-VCH, Weinheim, 2010.

[2] Z. Wu, D. Zhao, Ordered mesoporous materials as adsorbents, Chem. Commun. 47 (2011) 3332-3338.

[3] F.A. Viva, M.M. Bruno, M. Jobbágy, H.R. Corti, Electrochemical characterization of PtRu nanoparticles supported on mesoporous carbon for methanol electrooxidation, J. Phys. Chem. C, 116 (2012) 4097-4104.

[4] E. de la Llave, V. Borgel, E. Zinigrad, F.-F. Chesneau, P. Hartmann, Y.-K. Sun, D. Aurbach, Study of the most relevant aspects related to hard carbons as anode materials for Na-ion batteries, compared with Li-ion systems, Isr. J. Chem. 55 (2015) 1260-1274.

[5] E. de la Llave, V. Borgel, K.-J. Park, J.-Y. Hwang, Y.-K. Sun, P. Hartmann, F.-F. Chesneau, D. Aurbach, Comparison between Na-Ion and Li-Ion cells: understanding the critical role of the cathodes stability and the anodes pretreatment on the cells behavior, ACS Appl. Mater. Interfaces 8 (2016) 1867-1875.

[6] D. Hirshberg, D. Sharon, E. de la Llave, M. Afri, A.A. Frimer, W.-J. Kwak, Y.-K. Sun, D. Aurbach, Feasibility of full (Li-Ion)–O_2 cells comprised of hard carbon anodes, ACS Appl. Mater. Interfaces 9 (2017) 4352-4361.

[7] D. Saha, K. E. Warren, A. K. Naskar, Soft-templated mesoporous carbons as potential materials for oral drug delivery, Carbon 71 (2014) 47-57.

[8] X. Huang, S. Wu, X. Du, Gated mesoporous carbon nanoparticles as drug delivery system for stimuli-responsive controlled release, Carbon 101 (2016) 135-162.

[9] X. Yuan, S-P. Zhuo, W. Xing, H-Y. Cui, X-D. Dai, X-M. Liu, Z-F. Yan, Aqueous dye adsorption on ordered mesoporous carbons, J. Coll. Interf. Sci. 310 (2007) 83–89.

[10] S. Hosseini , T. S. Y. Choong, M. Hamid, Adsorption of a cationic dye from aqueous solution on mesoporous carbon-based honeycomb monolith, Desalin. Water Treat. 49 (2012) 326–336.

[11] R. Otero, D. Esquivel, M. A. Ulibarri, F. J. Romero-Salguero, P. Van Der Voort, J. M. Fernández, Mesoporous phenolic resin and mesoporous carbon for the removal of S-

Metolachlor and Bentazon herbicides, Chem. Eng. J. 251 (2014) 92-101.

[12] M. Naushad, T.Ahamad, B. M. Al-Maswari, A. A. Alqadami, S. M. Alshehri, Nickel ferrite bearing nitrogen-doped mesoporous carbon as efficient adsorbent for the removal of highly toxic metal ion from aqueous medium, Chem. Eng. J. 330 (2017) 1351-1360.

[13] J. Peng, W. Zhang, Y. Liu, Y. Jiang, L. Ni, J. Qiu, Superior adsorption performance of mesoporous carbon nitride for methylene blue and the effect of investigation of different modifications on adsorption capacity, Water Air Soil Pollut 228 (2017) 9 DOI 10.1007/s11270-016-3189-0.

[14] H. Gai, K. Guo, M. Xiao, N. Zhang, Z. Li, Z. Lv, H. Song, Ordered mesoporous carbons as highly efficient absorbent for coal gasification wastewater - A real case study based on the Inner Mongolia Autonomous coal gasification wastewater, Chem. Eng. J. 341 (2018) 471-482.

[15] C. Liang, Z. Li, S. Dai, Mesoporous carbon materials: synthesis and modification, Angew. Chem. Int. Ed. 47 (2008) 3696-3717.

[16] A. Stein, Z. Wang, M.A. Fierke, Functionalization of porous carbon materials with designed pore architecture, Adv. Mater. 21 (2009) 265-293.

[17] W. Li, J. Liu, D. Zhao, Mesoporous materials for energy conversion and storage devices, Nat. Rev. Mater. 1 (2016) 1-17.

[18] N.D. Petkovich, A. Stein, Controlling macro- and mesostructures with hierarchical porosity through combined hard and soft templating, Chem. Soc. Rev. 42 (2013) 3721-3739.

[19] S. Dutta, A. Bhaumik, K.C.W. Wu, Hierarchically porous carbon derived from polymers and biomass: effect of interconnected pores on energy applications, Energ. Environ. Sci. 7 (2014) 3574-3592.

[20] J. Xie, X. Yao, Q. Cheng, I.P. Madden, P. Dornath, C.-C. Chang, W. Fan, D. Wang, Three dimensionally ordered mesoporous carbon as a stable, high-performance Li–O_2 battery cathode, Angew. Chem. 127 (2015) 4373-4377.

[21] H.-D. Lim, H. Song, J. Kim, H. Gwon, Y. Bae, K.-Y. Park, J. Hong, H. Kim, T. Kim, Y.H. Kim, X. Lepró, R. Ovalle-Robles, R.H. Baughman, K. Kang, Superior rechargeability and efficiency of lithium–oxygen batteries: hierarchical air electrode architecture combined with a soluble catalyst, Angew. Chem. Int. Ed. 53 (2014) 3926-3931.

[22] H. Zhou, D. Wang, A. Fu, X. Liu, Y. Wang, Y. Li, P. Guo, H. Li, X.S. Zhao, Mesoporous carbon spheres with tunable porosity prepared by a template-free method for advanced lithium–sulfur batteries, Mater. Sci. Eng. B 227 (2018) 9-15.

[23] F. Rodríguez-Reinoso, M. Molina-Sabio, Activated carbons from lignocellulosic materials by chemical and/or physical activation: an overview, Carbon 30 (1992) 1111-1118.

[24] M.A. Lillo-Ródenas, J. Juan-Juan, D. Cazorla-Amorós, A. Linares-Solano, About reactions occurring during chemical activation with hydroxides, Carbon 42 (2004) 1371-1375.

[25] Y. Meng, D. Gu, F. Zhang, Y. Shi, L. Cheng, D. Feng, Z. Wu, Z. Chen, Y. Wan, A. Stein, D. Zhao, A family of highly ordered mesoporous polymer resin and carbon structures from organic-organic self-assembly, Chem. Mater. 18 (2006) 4447-4464.

[26] M.M. Bruno, N.G. Cotella, M.C. Miras, C.A. Barbero, A novel way to maintain resorcinol–formaldehyde porosity during drying: Stabilization of the sol–gel nanostructure using a cationic polyelectrolyte, Colloids Surf. A: Physicochem. Eng. Asp. 362 (2010) 28-32.

[27] M.M. Bruno, E.A. Franceschini, F.A. Viva, Y.R.J. Thomas, H.R. Corti,

Electrodeposited mesoporous platinum catalysts over hierarchical carbon monolithic support as anode in small PEM fuel cells, Int. J. Hydrog. Energy 37 (2012) 14911-14919.

[28] M.M. Bruno, F.A. Viva, M.A. Petruccelli, H.R. Corti, Platinum supported on mesoporous carbon as cathode catalyst for direct methanol fuel cells, J. Power Sources 278 (2015) 458-463.

[29] J.H. Knox, B. Kaur, G.R. Millward, Structure and performance of porous graphitic carbon in liquid chromatography, J. Chromatogr. A 352 (1986) 3-25.

[30] R. Ryoo, S.H. Joo, S. Jun, Synthesis of highly ordered carbon molecular sieves via template-mediated structural transformation, J. Phys. Chem. B 103 (1999) 7743-7746.

[31] A.H. Lu, F. Schüth, Nanocasting: a versatile strategy for creating nanostructured porous materials, Adv. Mater. 18 (2006) 1793-1805.

[32] K.P. Gierszal, T.-W. Kim, R. Ryoo, M. Jaroniec, Adsorption and structural properties of ordered mesoporous carbons synthesized by using various carbon precursors and ordered siliceous P6mm and Ia3̄d mesostructures as templates, J. Phys. Chem. B 109 (2005) 23263-23268.

[33] T.-W. Kim, R. Ryoo, K.P. Gierszal, M. Jaroniec, L.A. Solovyov, Y. Sakamoto, O. Terasaki, Characterization of mesoporous carbons synthesized with SBA-16 silica template, J. Mater. Chem. 15 (2005) 1560-1571.

[34] P. Zhang, H. Zhu, S. Dai, Porous carbon supports: recent advances with various morphologies and compositions, ChemCatChem 7 (2015) 2788-2805.

[35] P. Karandikar, K.R. Patil, A. Mitra, B. Kakade, A.J. Chandwadkar, Synthesis and characterization of mesoporous carbon through inexpensive mesoporous silica as template, Microporous Mesoporous Mater. 98 (2007) 189-199.

[36] M. Sevilla, P. Valle-Vigón, P. Tartaj, A.B. Fuertes, Magnetically separable bimodal

mesoporous carbons with a large capacity for the immobilization of biomolecules, Carbon 47 (2009) 2519-2527.

[37] J. Lee, J. Kim, T. Hyeon, A facile synthesis of bimodal mesoporous silica and its replication for bimodal mesoporous carbon, Chem. Commun. (2003) 1138-1139.

[38] W. Huang, J. Chong, Y. Tian, X. Wang, Acid-programmed control of dual-mesoporous carbon nanospheres with predictable diameter, Chem. Eng. J. 327 (2017) 18-27.

[39] S.J. Gregg, K.S.W. Sing, Adsorption, surface area, and porosity, Academic Press, New York 1991.

[40] S. Brunauer, P.H. Emmett, E. Teller, Adsorption of gases in multimolecular layers, J. Am. Chem. Soc. 60 (1938) 309-319.

[41] E.P. Barrett, L.G. Joyner, P.P. Halenda, The determination of pore volume and area distributions in porous substances. I. computations from nitrogen isotherms, J. Am. Chem. Soc. 73 (1951) 373-380.

[42] O. Paris, C. Zollfrank, G.A. Zickler, Decomposition and carbonisation of wood biopolymers—a microstructural study of softwood pyrolysis, Carbon 43 (2005) 53-66.

[43] Boehm H, Surface chemical characterization of carbons from adsorption studies. In: Bottani, E. J., Tascón, J. M. D., Eds., Adsorption by carbons, Amsterdam: Elsevier; 2008. pp. 301–327.

[44] S. L. Goertzen, K. D. Thériault, A. M. Oickle, A. C. Tarasuk, H. A. Andreas, Standardization of the Boehm titration. Part I. CO_2 expulsion and endpoint determination. Carbon 48 (2010) 1252-1261.

[45] A. M. Oickle, S. L., Goertzen, K. R. Hopper, Y. O. Abdalla, H. A. Andreas, Standardization of the Boehm titration: Part II. Method of agitation, effect of filtering and

dilute titrant. Carbon 48 (2010) 3313-3322.

[46] K. Kinoshita, Carbon: electrochemical and physicochemical properties, Wiley, United States 1988.

[47] Evonik, http://www.aerosil.com/product/aerosil/downloads/ii-2242-inorganic-materials-for-catalyst-innovation-en.pdf, Access date 04/05/2018.

[48] M. Thommes, K. Kaneko, V. Neimark Alexander, P. Olivier James, F. Rodriguez-Reinoso, J. Rouquerol, S.W. Sing Kenneth, Physisorption of gases, with special reference to the evaluation of surface area and pore size distribution (IUPAC Technical Report), Pure Appl. Chem. 87 (2015) 1051-1069.

[49] Y.R.J. Thomas, M.M. Bruno, H.R. Corti, Characterization of a monolithic mesoporous carbon as diffusion layer for micro fuel cells application, Microporous Mesoporous Mater. 155 (2012) 47-55.

[50] B. Tian, X. Ge, G. Pan, B. Fan, Z. Luan, Adsorption and flocculation behaviors of polydiallyldimethylammonium (PDADMA) salts: Influence of counterion, Int. J. Miner. Process. 79 (2006) 209-216.

[51] S.H. Behrens, D.G. Grier, The charge of glass and silica surfaces, J. Chem. Phys. 115 (2001) 6716-6721.

[52] H. Dautzenberg, E. Görnitz, W. Jaeger, Synthesis and characterization of poly(diallyldimethyl ammonium chloride) in a broad range of molecular weight, Macromol. Chem. Phys. 199 (1998) 1561-1571.

[53] R.V. Klitzing, B. Kolaric, W. Jaeger, A. Brandt, Structuring of poly(DADMAC) chains in aqueous media: a comparison between bulk and free-standing film measurements, Phys. Chem. Chem. Phys. 4 (2002) 1907-1914.

[54] C. Lin, J.A. Ritter, Effect of synthesis pH on the structure of carbon xerogels, Carbon

35 (1997) 1271-1278.

[55] J. Jin, S. Tanaka, Y. Egashira, N. Nishiyama, KOH activation of ordered mesoporous carbons prepared by a soft-templating method and their enhanced electrochemical properties, Carbon 48 (2010) 1985-1989.

[56] G.S. Chai, S.B. Yoon, J.-S. Yu, J.-H. Choi, Y.-E. Sung, Ordered porous carbons with tunable pore sizes as catalyst supports in direct methanol fuel cell, J. Phys. Chem. B 108 (2004) 7074-7079.

[57] T. Horikawa, T. Sekida, J. Hayashi, M. Katoh, D. D. Do, A new adsorption–desorption model for water adsorption in porous carbons, Carbon 49 (2011) 416-424.

[58] A. Reffas, V. Bernardet, B. David, L. Reinert, M. Bencheikh Lehocine, M. Dubois, N. Batisse, L. Duclaux, Carbons prepared from coffee grounds by H_3PO_4 activation: Characterization and adsorption of methylene blue and Nylosan Red N-2RBL, J. Hazard. Mater. 175 (2010) 779-788.

[59] A. Delgado, F. González-Caballero, J. M. Bruque. On the zeta potential and surface charge density of montmorillonite in aqueous electrolyte solutions, J. Coll. Interf. Sci. 113 (1986) 203-211.

[60] C. Pardanaud, C. Martin, P. Roubin, G. Giacometti, C. Hopf, T. Schwarz-Selinger, W. Jacob, Raman spectroscopy investigation of the H content of heated hard amorphous carbon layers, Diamond Relat. Mater. 34 (2013) 100-104.

[61] O. Beyssac, J.-N. Rouzaud, B. Goffé, F. Brunet, C. Chopin, Graphitization in a high-pressure, low-temperature metamorphic gradient: a Raman microspectroscopy and HRTEM study, Contrib. Mineral. Petrol. 143 (2002) 19-31.

[62] J. Ribeiro-Soares, M.E. Oliveros, C. Garin, M.V. David, L.G.P. Martins, C.A.

Almeida, E.H. Martins-Ferreira, K. Takai, T. Enoki, R. Magalhães-Paniago, A. Malachias, A. Jorio, B.S. Archanjo, C.A. Achete, L.G. Cançado, Structural analysis of polycrystalline graphene systems by Raman spectroscopy, Carbon 95 (2015) 646-652.

[63] G. Li, Z. Lu, B. Huang, Z. Wang, H. Huang, R. Xue, L. Chen, Raman scattering investigation of carbons obtained by heat treatment of a polyfurfuryl alcohol, Solid State Ionics 89 (1996) 327-331.

[64] A.C. Ferrari, J. Robertson, Interpretation of Raman spectra of disordered and amorphous carbon, Phys. Rev. B 61 (2000) 14095-14107.

[65] A. Cuesta, P. Dhamelincourt, J. Laureyns, A. Martínez-Alonso, J.M.D. Tascón, Raman microprobe studies on carbon materials, Carbon 32 (1994) 1523-1532.

[66] Y. Liu, J.S. Xue, T. Zheng, J.R. Dahn, Mechanism of lithium insertion in hard carbons prepared by pyrolisis of epoxy resins, Carbon 34 (1996) 193-200.

[67] T. Zheng, W. Xing, J.R. Dahn, Carbons prepared from coals for anodes of lithium ion cells, Carbon 34 (1996) 1501-1507.

[68] L.G. Jacobsen, G. Capote, M.E.H. Maia da Costa, D.F. Franceschini, F.L. Freire Jr., Nanoporosity in plasma deposited amorphous carbón films investigated by small-angle X-ray scattering, Diam. Rel. Mater. 11 (2002) 1946-1951.

[69] B.K. Ostaflychuk, V.I. Mandzyuk, Y.O. Kulik, N.I. Nagirna, SAXS investigation of nanoporous structure of thermal modified carbon materials, Nanoscale Res. Lett. 9 (2014) 160.

[70] G. G. Stavropoulos, A. A. Zabaniotou, Production and characterization of activated carbons from olive-seed waste residue, Microp. Mesop. Mater. 82 (2005) 79-85.

[71] B. Bestani, N. Benderdouche, B. Benstaali, M. Belhakem, A. Addou, Methylene blue and iodine adsorption onto an activated desert plant. Biores. Techn. 99 (2008), 8441-8444.

[72] M. J. Avena, L. E. Valenti, V. Pfaffen, C. P de Pauli, Methylene blue dimerization does not interfere in surface-area measurements of kaolinite and soils, Clays Clay Miner. 49 (2001) 168-173.

[73] C. Yan, C. Wang, J. Yao, L. Zhang, X. Liu, Adsorption of methylene blue on mesoporous carbons prepared using acid- and alkaline-treated zeolite X as the template, Colloids Surf. A 333 (2009) 115-119.

[74] K. Jedynak, M. Repelewicz, Adsorption of methylene blue and malachite green on micro-mesoporous carbon materials, Adsorp. Sci. Techn. 35 (2017) 499–506.

[75] Q. Zhou, X. Jiang, Y. Guo, G. Zhang, W. Jiang, An ultra-high surface area mesoporous carbon prepared by a novel MnO-templated method for highly effective adsorption of methyleneblue, Chemosphere 201 (2018) 519-529.

[76] S. Hosseini, T. S. Y. Choong, M. Hamid, Adsorption of a cationic dye from aqueous solution on mesoporous carbon-based honeycomb monolith, Desalin. Water Treat. 49 (2012) 326–336.

[77] F. Marrakchi, M. Auta, W.A. Khanday, B. H. Hameed, High-surface-area and nitrogen-rich mesoporous carbon material from fishery waste for effective adsorption of methylene blue, Powder Techn. 321 (2017) 428–434.

[78] X. Yuan, S-P. Zhuo, W. Xing, H-Y. Cui, X-D. Dai, X-M. Liu, Z-F. Yan, Aqueous dye adsorption on ordered mesoporous carbons, J. Coll. Interf. Sci. 310 (2007) 83–89.

[79] Y. Liu, G. Zeng, L. Tang, Y. Cai, Y. Pang, Y. Zhang, G. Yang, Y. Zhou, X. He, Y. He, Highly effective adsorption of cationic and anionic dyes on magnetic Fe/Ni nanoparticles doped bimodal mesoporous carbon, J. Coll. Interf. Sci. 448 (2015) 451–459.

[80] J. Peng, W. Zhang, Y. Liu, Y. Jiang, L. Ni, J. Qiu, Superior adsorption performance of mesoporous carbon nitride for methylene blue and the effect of investigation of different

modifications on adsorption capacity, Water Air Soil Pollut 228 (2017) 9 DOI 10.1007/s11270-016-3189-0.

[81] K. Legrouria, E. Khouyab, M. Ezzinea, H. Hannachea, R. Denoyelc, R. Pallierd, R. Naslain, Production of activated carbon from a new precursor molasses by activation with sulphuric acid, J. Hazard. Mater. B 118 (2005) 259-263.

[82] G. Karaçetin, S. Sivrikaya, M. Imamoğlu, Adsorption of methylene blue from aqueous solutions by activated carbon prepared from hazelnut husk using zinc chloride, J. Anal. Appl. Pyrol. 110 (2014) 270-276.

[83] G. G. Stavropoulos, A. A. Zabaniotou, Production and characterization of activated carbons from olive-seed waste residue, Microporous Mesoporous Mater. 82 (2005) 79-85.

[84] A. L. Ahmad, M. M. Loh, A. J. Aziz, Preparation and characterization of activated carbon from oil palm wood and its evaluation on methylene blue adsorption, Dyes Pigments 75 (2007) 263-272.

[85] E. N. El Qada, J.A., S. J. Allen, G. A. Walker, Adsorption of basic dyes from aqueous solution onto activated carbons, Chem. Eng. J. 135 (2008) 174-184

[86] G. Duman, Y. Onal, C. Okutucu, S. Onenc, J. Yanik, Production of activated carbon from pine cone and evaluation of its physical, chemical, and adsorption properties, Energy Fuel 23 (2009) 2197-2204.

[87] K. C. Bedin, A. C. Martins, A. L. Cazetta, O. Pezoti, V. C. Almeida, KOH-activated carbon prepared from sucrose spherical carbon: adsorption equilibrium, kinetic and thermodynamic studies for methylene blue removal, Chem. Eng. J. 286 (2016) 476-484.

[88] T. Liu, Y. Li, Q. Du, J. Sun, Y. Jiao, G. Yang, Z. Wang, Y. Xia, W. Zhang, K. Wang, H. Zhu, D. Wu, Adsorption of methylene blue from aqueous solution by grapheme, Colloids Surf. B 90 (2012) 197-203.

[89] Y. Yao, F. Xu, M. Chen, Z. Xu, Z. Zhu, Absorption behavior of methylene blue on carbon nanotubes, Biores. Technol. 101 (2010) 3040-3046.

[90] J. Ma, F. Yu, L. Zhou, L. Jin, M. Yang, J. Luan, Y. Tang, H. Fan, Z. Yuan, J. Chen, Enhanced adsorptive removal of methyl orange and methylene blue from aqueous solution by alkali-activated multiwalled carbon nanotubes, ACS Appl. Mater. Interfaces 4 (2012) 5749-5760.

[91] S. Zhang, M. Zeng, J. Li, J. Li, J. Xu, X. Wang, Porous magnetic carbon sheets from biomass as an adsorbent for the fast removal of organic pollutants from aqueous solution, J. Mater. Chem. A, 2 (2014) 4391-4397.

[92] A. M. M. Vargas, A. L. Cazetta, M. H. Kunita, T. L. Silva, V. C. Almeida, Adsorption of methylene blue on activated carbon produced from flamboyant pods (Delonix regia): Study of adsorption isotherms and kinetic models, Chem. Eng J. 108 (2011) 722-730.

[93] S. Langergren, B. K. Svenska, Zur theorie der sogenannten adsorption geloster stoffe, Kungl. Svenska Vetenskapsakad. Handl. 28 (1898) 1-39.

[94] G. McKay, Y. S. Ho, Pseudo-second-order model for sorption processes, Process. Biochem. 34 (1999) 451-465.

[95] W.J. Weber, J.C. Morris, Kinetics of adsorption on carbon from solution**,** J. Sanitary Eng. Div. 89 (1963) 31-60.

[96] I.A. W. Tan, A. L. Ahmad, B. H. Hameed, Enhancement of basic dye adsorption uptake from aqueous solutions using chemically modified oil palm shell activated carbon, Coll. Surf. A 318 (2008) 88-96.

[97] D. Kavitha, C. Namasivayam, Experimental and kinetic studies on methylene blue adsorption by coir pith carbon, Bioresour. Technol. 98 (2007) 14–21.

[98] B. Hameed, A. Ahmad, K. Latiff, Adsorption of basic dye (methylene blue) onto activated carbon prepared from rattan sawdust, Dyes Pigments 75 (2007) 143–149.

[99] F-C. Wu, R-L. Tseng, R-S. Juang, Initial behavior of intraparticle diffusion model used in the description of adsorption kinetics, Chem. Eng. J. 153 (2009) 1-8.

Table 1. RF resin volume, pore volume of silica, and their ratio.

Sample	V_R(cm^3)	V_S(cm^3)	V_R/V_S	Sample	V_R(cm^3)	V_S(cm^3)	V_R/V_S
$P_{04}S_{00}$	5.08	0.00	∞	$P_{04}S_{15}$	4.95	5.71	0.87
$P_{04}S_{01}$	5.06	0.38	13.37	$P_{04}S_{20}$	5.14	7.72	0.67
$P_{04}S_{02}$	5.60	0.79	7.05	$P_{04}S_{30}$	5.12	11.54	0.44
$P_{04}S_{05}$	5.08	1.89	2.68	$P_{04}S_{60}$	4.43	23.27	0.19
$P_{04}S_{10}$	5.02	3.78	1.33	$P_{00}S_{20}$	5.20	7.72	0.67

Table 2. Specific and surface concentration of different functional groups.

Group	$P_{04}S_{00}$		$P_{04}S_{30}$		$P_{00}S_{20}$	
	$\mu mol \cdot g^{-1}$	$\mu mol \cdot m^{-2}$	$\mu mol \cdot g^{-1}$	$\mu mol \cdot m^{-2}$	$\mu mol \cdot g^{-1}$	$\mu mol \cdot m^{-2}$
Phenolic	113 ± 3	0.17 ± 0.04	166 ± 4	0.17 ± 0.04	117 ± 3	0.15 ± 0.04
Lactonic	14 ± 2	0.021 ± 0.001	14 ± 2	0.014 ± 0.001	18 ± 2	0.024 ± 0.001
Carboxylic	80 ± 3	0.12 ± 0.04	87 ± 3	0.09 ± 0.04	94 ± 3	0.13 ± 0.04
Total	207 ± 8	0.31 ± 0.08	267 ± 9	0.27 ± 0.08	229 ± 8	0.30 ± 0.08

Table 3. Raman deconvolution parameters.

Sample	V_R/V_S	D band (cm^{-1})	G band (cm^{-1})	I_D/I_G	$I_D/(I_D+I_G)$
$P_{04}S_{00}$	∞	1354	1600	2.21	0.69
$P_{04}S_{01}$	13.37	1349	1604	2.07	0.67
$P_{04}S_{05}$	2.68	1352	1602	2.67	0.73
$P_{04}S_{15}$	0.87	1348	1599	1.79	0.64
$P_{04}S_{30}$	0.44	1350	1604	2.19	0.69

Table 4. Hard carbons parameters obtained by XRD.

Sample	V_R/V_S	d_{002} (nm)	Lc (nm)	Lc/d_{002}	R	La (nm)
$P_{04}S_{00}$	∞	0.392	0.96	2.4	1.78	3.45
$P_{04}S_{01}$	13.37	0.388	1.05	2.7	1.73	2.95
$P_{04}S_{05}$	2.68	0.385	0.94	2.5	1.96	3.53
$P_{04}S_{15}$	0.87	0.377	0.89	2.4	1.95	3.61
$P_{04}S_{30}$	0.44	0.376	1.19	3.2	1.74	3.45

Table 5. Isotherm parameters for MB adsorbed onto mesoporous carbons.

Sample	Langmuir equation			Freundlich equation		
	q_m (mg·g^{-1})	K_L (dm^3·mg^{-1})	R^2	K_F (dm^3·g^{-1})	n	R^2
$P_{04}S_{02}$	319 ± 7	0.042 ± 0.004	0.990	84 ± 18	4.48 ± 0.87	0.826
$P_{04}S_{60}$	431 ± 9	0.37 ± 0.05	0.975	292 ± 20	13.6 ± 2.7	0.841

Table 6. Pseudo second order parameters for the adsorption of MB onto mesoporous carbon.

Sample	A_{tot} ($m^2 \cdot g^{-1}$)	A_{mic} ($m^2 \cdot g^{-1}$)	V_{tot} ($cm^3 \cdot g^{-1}$)	V_{mic} ($cm^3 \cdot g^{-1}$)	d_p (nm)	q_e ($mg \cdot g^{-1}$)	k_2 (min^{-1})	R^2
$P_{04}S_{60}$	950	176	2.10	0.02	4.5/30	98.1 ± 0.1	$(1.8 \pm 0.6)x10^4$	0.9999
$P_{04}S_{30}$	998	212	1.70	0.04	4.5/25	98.0 ± 0.1	$(3.5 \pm 0.9)\ x10^3$	0.9999
$P_{00}S_{20}$	745	399	0.70	0.13	9	101.0 ± 0.3	78 ± 7	0.9999
$P_{04}S_{02}$	717	438	1.09	0.15	21	96.1 ± 0.4	66 ± 8	0.9998
$P_{04}S_{00}$	662	401	0.75	0.13	16	96.1 ± 0.4	64 ± 9	0.9998

Table 7. Intraparticle diffusion parameters for the adsorption of MB onto mesoporous carbon.

Sample	k_1 ($min^{-1/2}$)	k_2 ($min^{-1/2}$)	k_3 ($min^{-1/2}$)	C_1 ($mg \cdot g^{-1}$)	C_2 ($mg \cdot g^{-1}$)	C_3 ($mg \cdot g^{-1}$)
P$_{04}$S$_{60}$	-	0.46	0.03	-	96.3	98.1
P$_{04}$S$_{30}$	5.24	0.76	0.01	87.2	95.7	98.9
P$_{00}$S$_{20}$	13.38	3.88	0.03	46.5	77.3	98.3
P$_{04}$S$_{02}$	11.20	2.81	0.20	49.2	75.5	92.5
P$_{04}$S$_{00}$	3.29	1.68	0.18	74.2	81.3	93.1

Figure captions

Figure 1. Scheme of the procedure for mesoporous carbon production.

Figure 2. a) N_2 adsorption-desorption isotherms of silica powder (Sipernat® 50) at 77 K; b) Pore size distribution.

Figure 3. a) N_2 adsorption-desorption isotherms at 77 K. The values on the right side correspond to the adsorption at $p/p^0 = 1$; b) pore size distribution from BJH (desorption branch) method; c) mesopore volume of the "$P_{04}S_y$" series of carbon samples (black: pore size < 10 nm, red: pore size > 10 nm, and green: total).

Figure 4. Pore size distribution (desorption branch) for sample $P_{04}S_{30}$, before (empty symbol) and after (fill symbol) removal of the silica hard template.

Figure 5. SEM images of samples $P_{04}S_{00}$ (a), $P_{00}S_{20}$ (b), and $P_{04}S_{30}$ (c). Magnification: x 400,000.

Figure 6. a) BET surface area, and micropore surface from t-plot model and b) total pore volume and micropore volume.

Figure 7. Raman spectra of the carbon samples showing the corresponding deconvoluted curves. The pink line represents the envelope of the fitted spectrum.

Figure 8. Powder X-ray diffraction patterns of the carbon samples.

Figure 9. SAXS patterns: scattered intensity as a function of the scattering vector modulus for the carbon samples $P_{04}S_{00}$ (green), $P_{04}S_{60}$ (red), and $P_{00}S_{20}$ (blue).

Figure 10. Experimental isotherm for the adsorption of MB onto the samples $P_{04}S_{02}$ (●) and $P_{04}S_{60}$ (▲). Dashed and dotted lines correspond to Langmuir and Freundlich isotherms fits, respectively.

Figure 11. Scheme of the pore architecture of bimodal mesoporous carbons with micropores.

Figure 12. Sorption of MB onto mesoporous carbon as a function of time. Typical errors bars (estimated from duplicate runs) are indicated for two samples.

Figure 13. Linear fits of the intraparticle diffusion equation for MB adsorption onto samples $P_{04}S_{00}$ (Δ), $P_{04}S_{02}$ (□), $P_{00}S_{20}$ (○), and $P_{04}S_{30}$ (∇), showing three kinetics regions: 1- red, 2- blue, and 3- black.

Highlights

Hierarchical carbons were successfully prepared by using double pore forming method.

Hard carbon powders from resorcinol-formaldehyde polymer carbonization were obtained.

Mesopores volume fraction can be modified by tuning the ratio of pDADMAC/silica used.

Hierarchical carbons exhibit high adsorption capacity and kinetic toward MB.

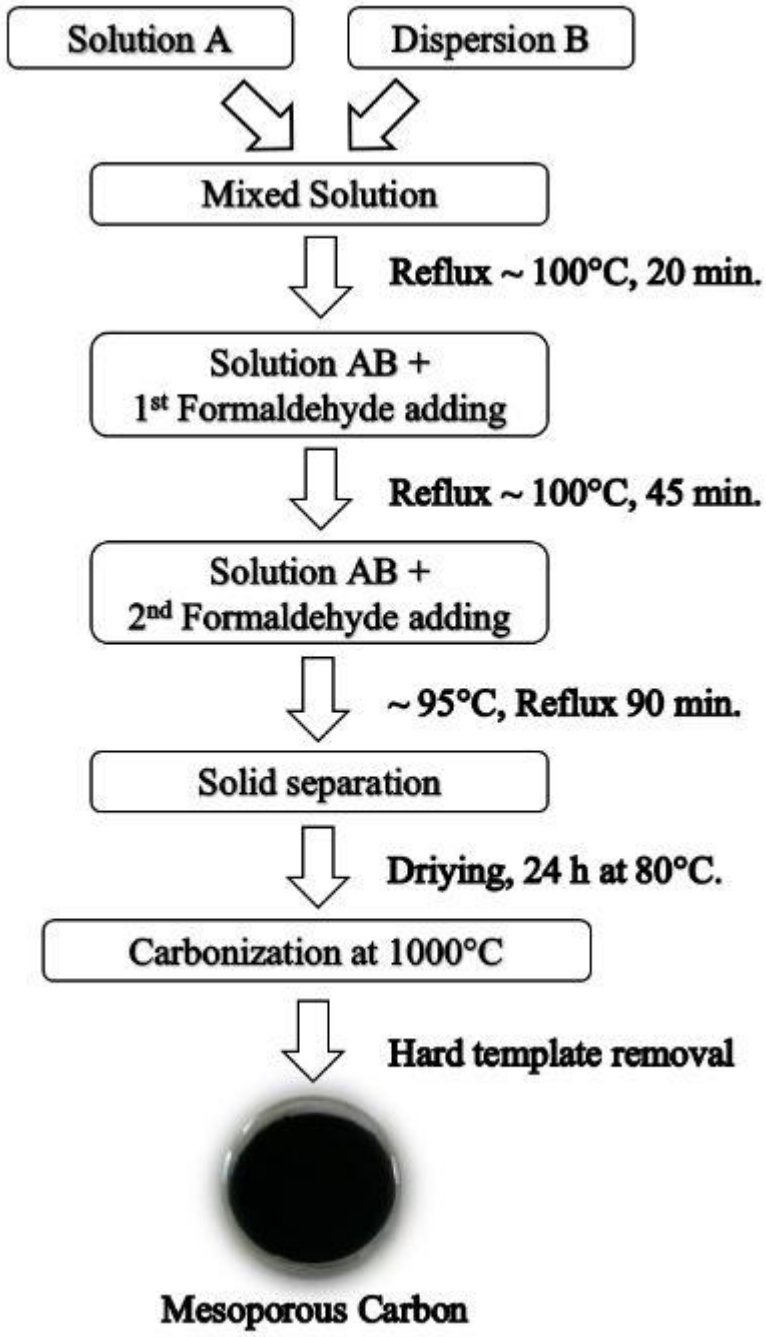
Solution A
Dispersion B
Mixed Solution
Reflux ~ 100°C, 20 min.
Solution AB +
1st Formaldehyde adding
Reflux ~ 100°C, 45 min.
Solution AB +
2nd Formaldehyde adding
~ 95°C, Reflux 90 min.
Solid separation
Driying, 24 h at 80°C.
Carbonization at 1000°C
Hard template removal
Mesoporous Carbon

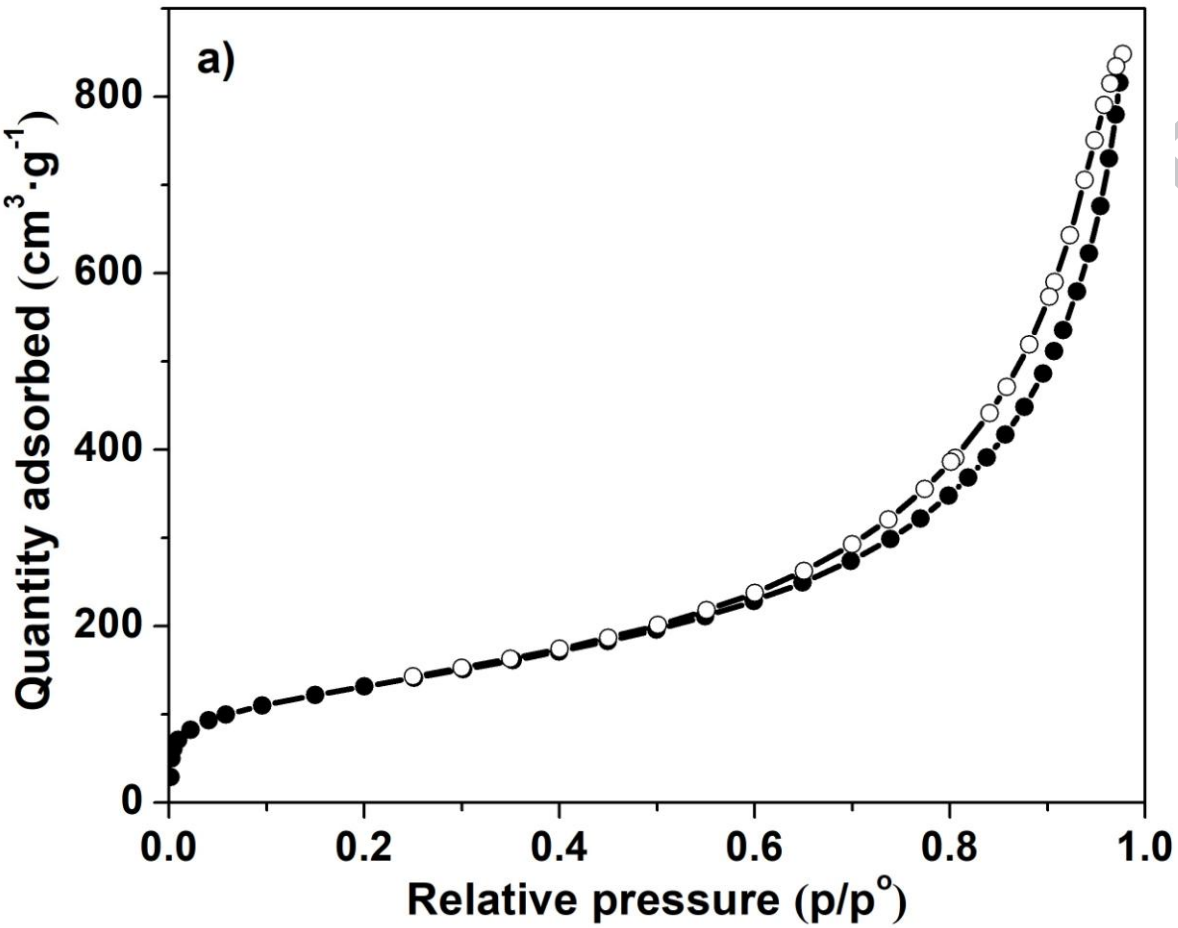
a)
Quantity adsorbed (cm^3·g^{-1})
800
600
400
200
0
0.0
0.2
0.4
0.6
0.8
1.0
Relative pressure (p/p°)

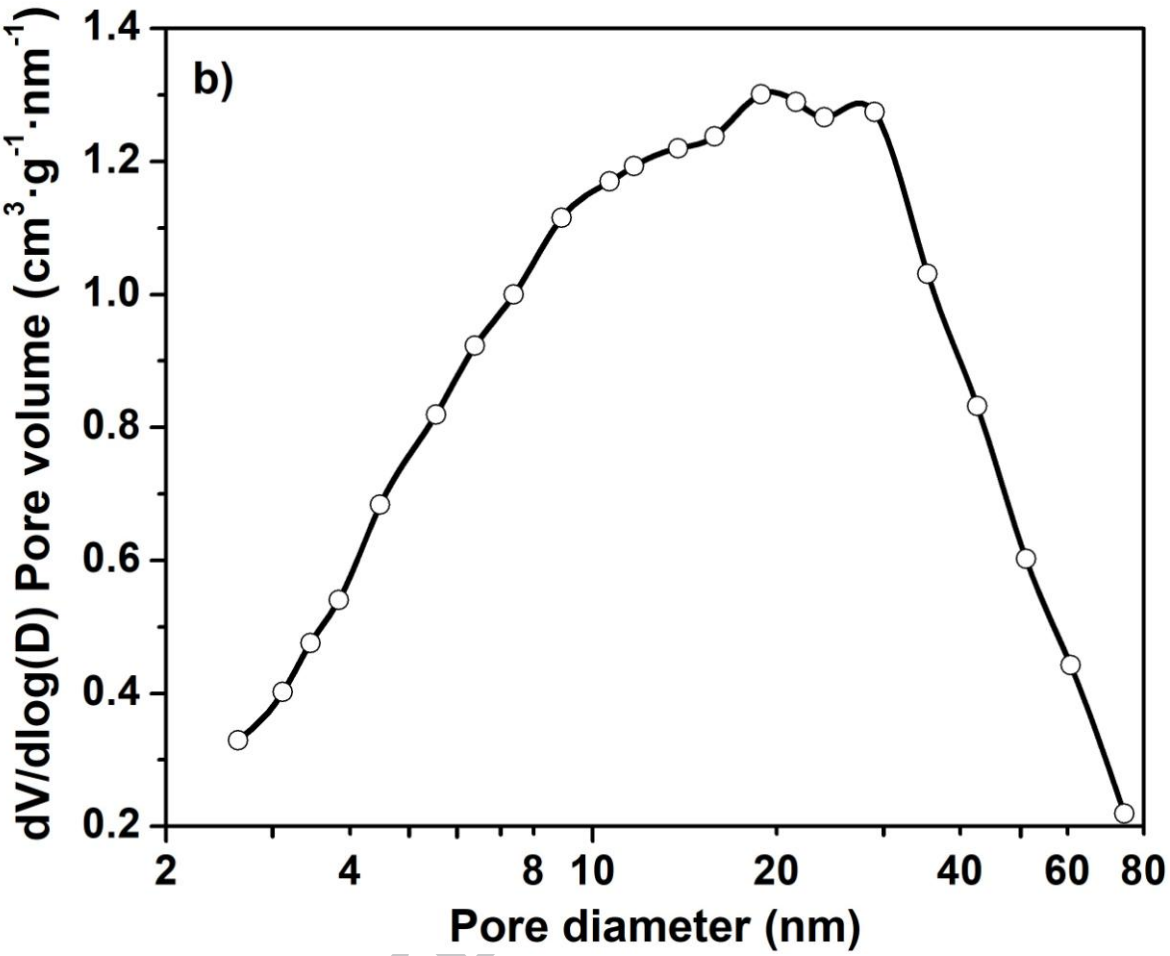
b)
dV/dlog(D) Pore volume (cm3·g-1·nm-1)
1.4
1.2
1.0
0.8
0.6
0.4
0.2
2
4
8
10
20
40
60
80
Pore diameter (nm)

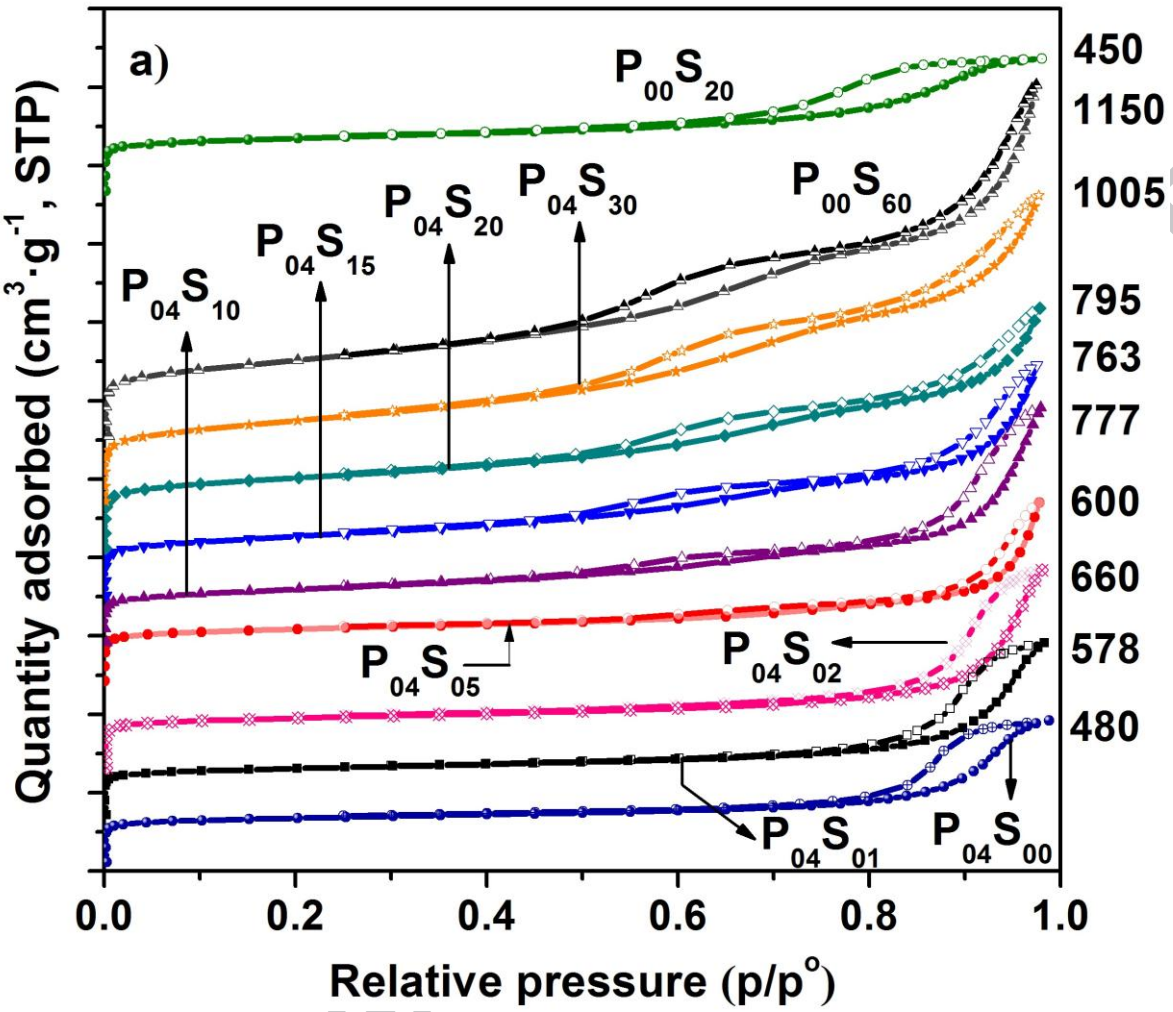
a)
$P_{00}S_{20}$
$P_{04}S_{30}$
$P_{04}S_{20}$
$P_{04}S_{15}$
$P_{04}S_{10}$
$P_{00}S_{60}$
$P_{04}S_{05}$
$P_{04}S_{02}$
$P_{04}S_{01}$
$P_{04}S_{00}$
450
1150
1005
795
763
777
600
660
578
480
Quantity adsorbed ($cm^3 \cdot g^{-1}$, STP)
0.0
0.2
0.4
0.6
0.8
1.0
Relative pressure (p/p^o)

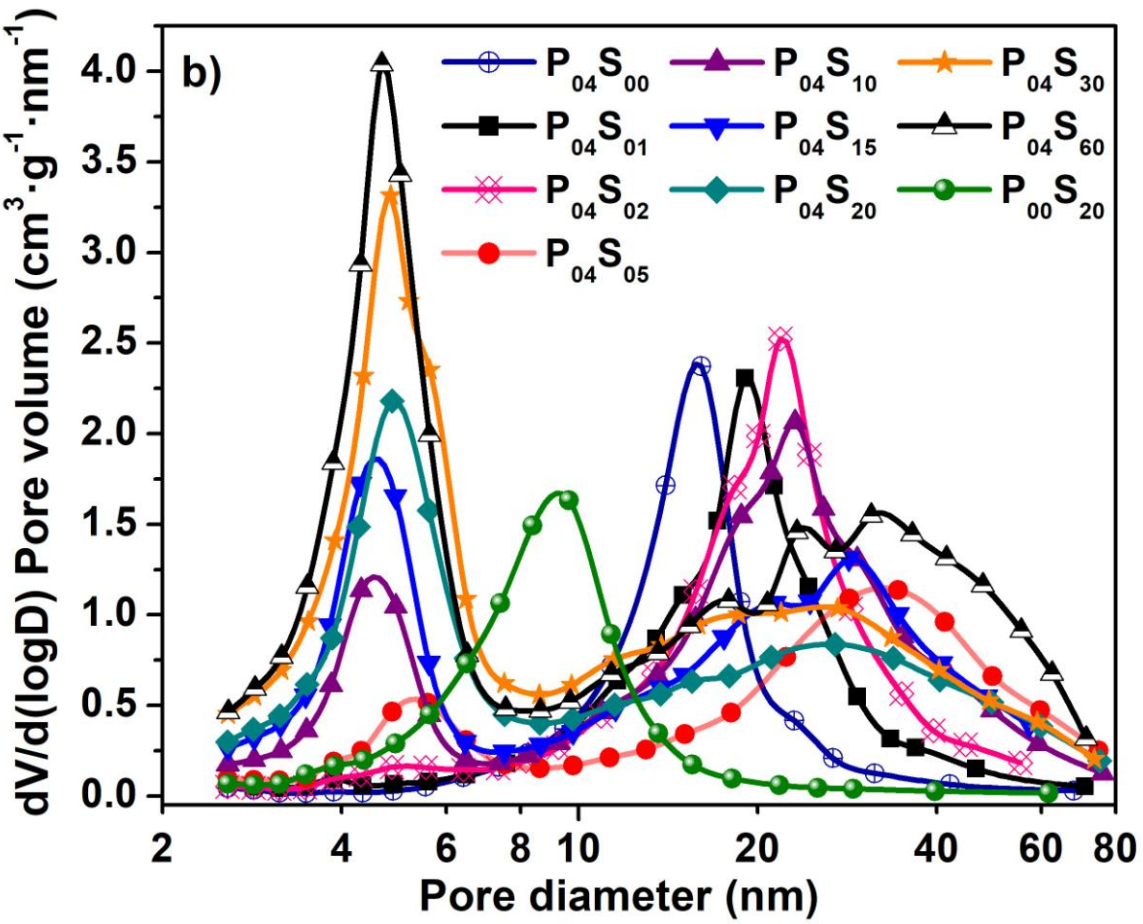
b)
$P_{04}S_{00}$
$P_{04}S_{10}$
$P_{04}S_{30}$
$P_{04}S_{01}$
$P_{04}S_{15}$
$P_{04}S_{60}$
$P_{04}S_{02}$
$P_{04}S_{20}$
$P_{00}S_{20}$
$P_{04}S_{05}$
dV/d(logD) Pore volume ($cm^3 \cdot g^{-1} \cdot nm^{-1}$)
0.0
0.5
1.0
1.5
2.0
2.5
3.0
3.5
4.0
2
4
6
8
10
20
40
60
80
Pore diameter (nm)

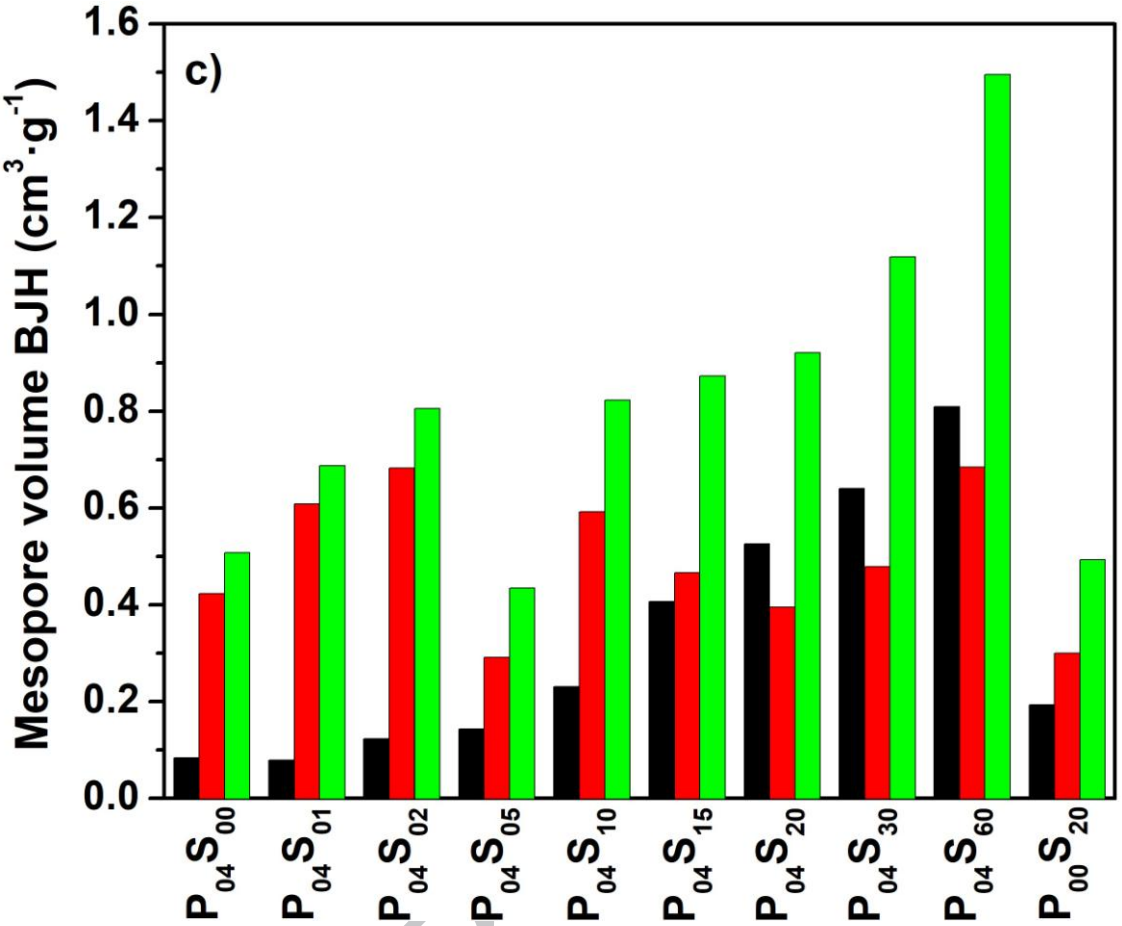
c)
Mesopore volume BJH (cm3·g-1)
1.6
1.4
1.2
1.0
0.8
0.6
0.4
0.2
0.0
P04S00
P04S01
P04S02
P04S05
P04S10
P04S15
P04S20
P04S30
P04S60
P00S20

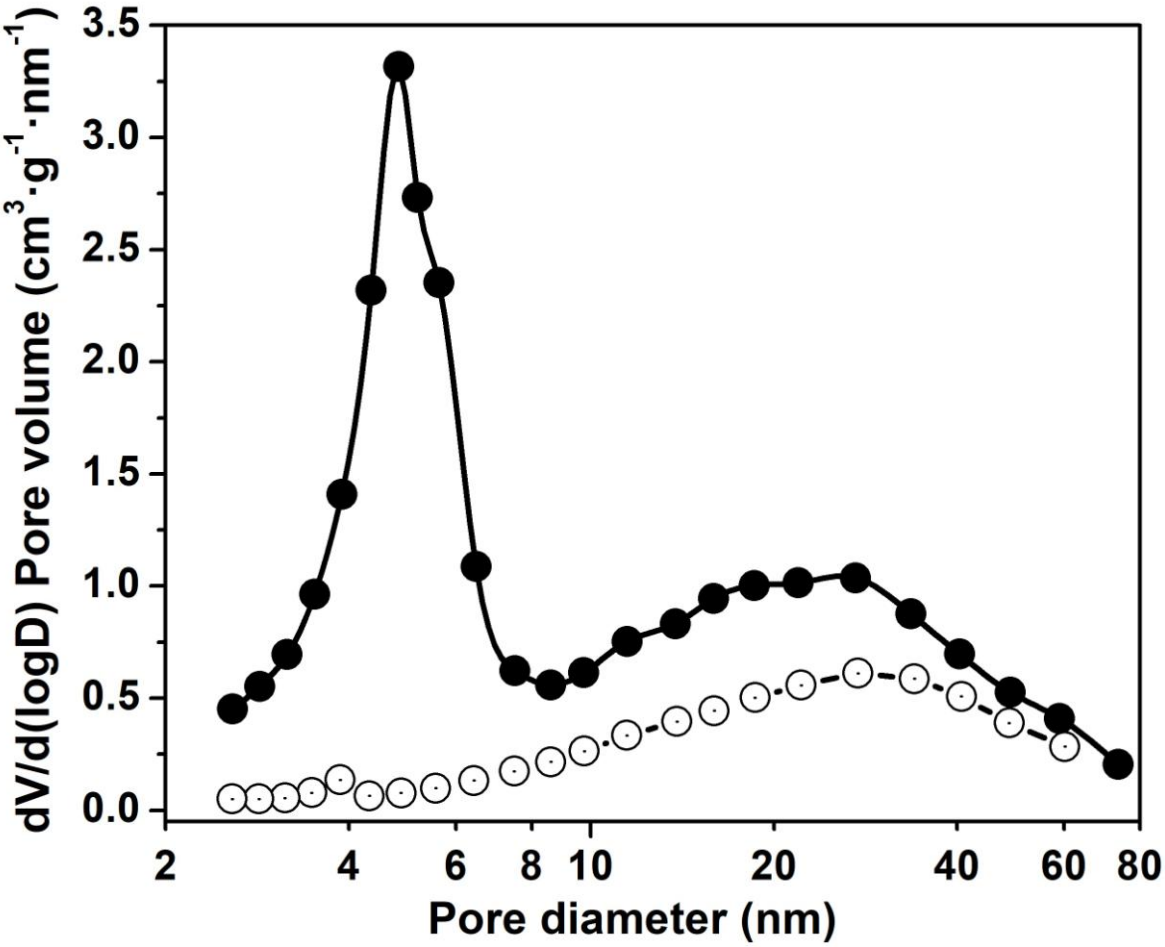
dV/d(logD) Pore volume (cm3·g-1·nm-1)
3.5
3.0
2.5
2.0
1.5
1.0
0.5
0.0
2
4
6
8
10
20
40
60
80
Pore diameter (nm)

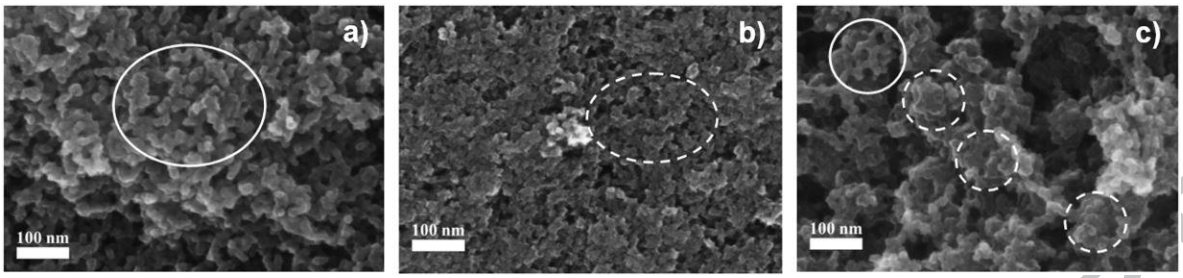

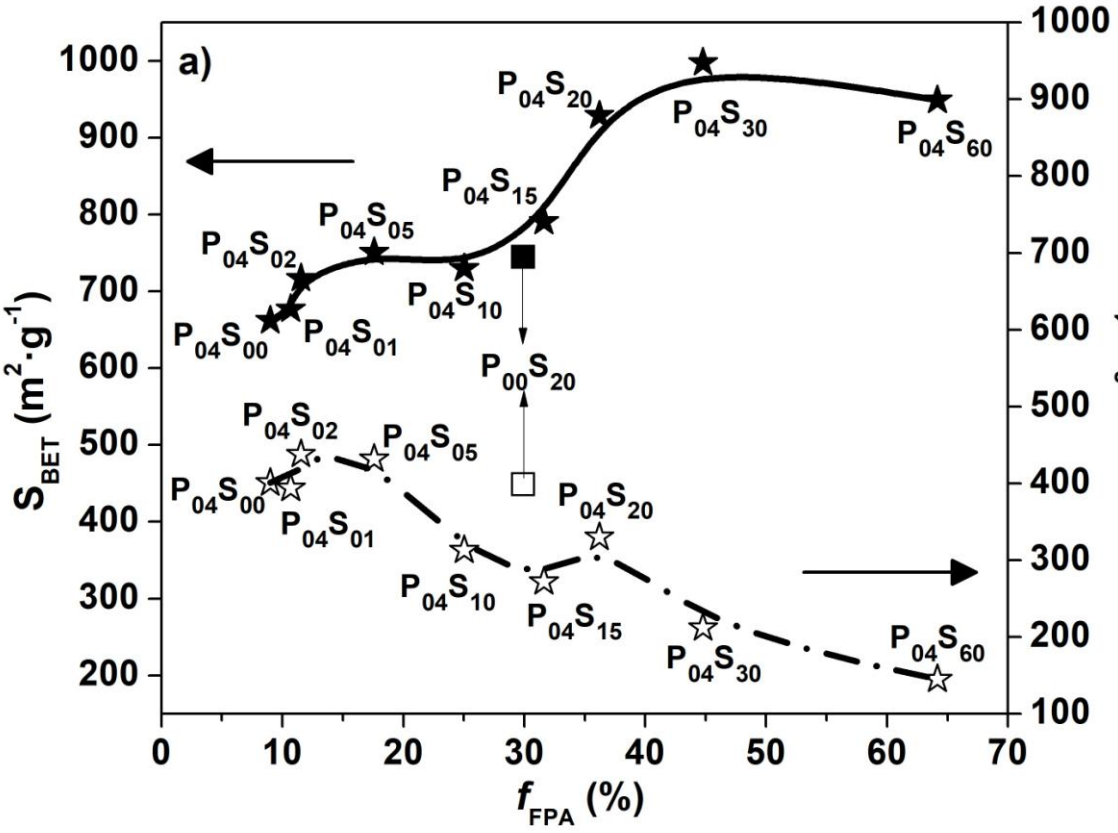

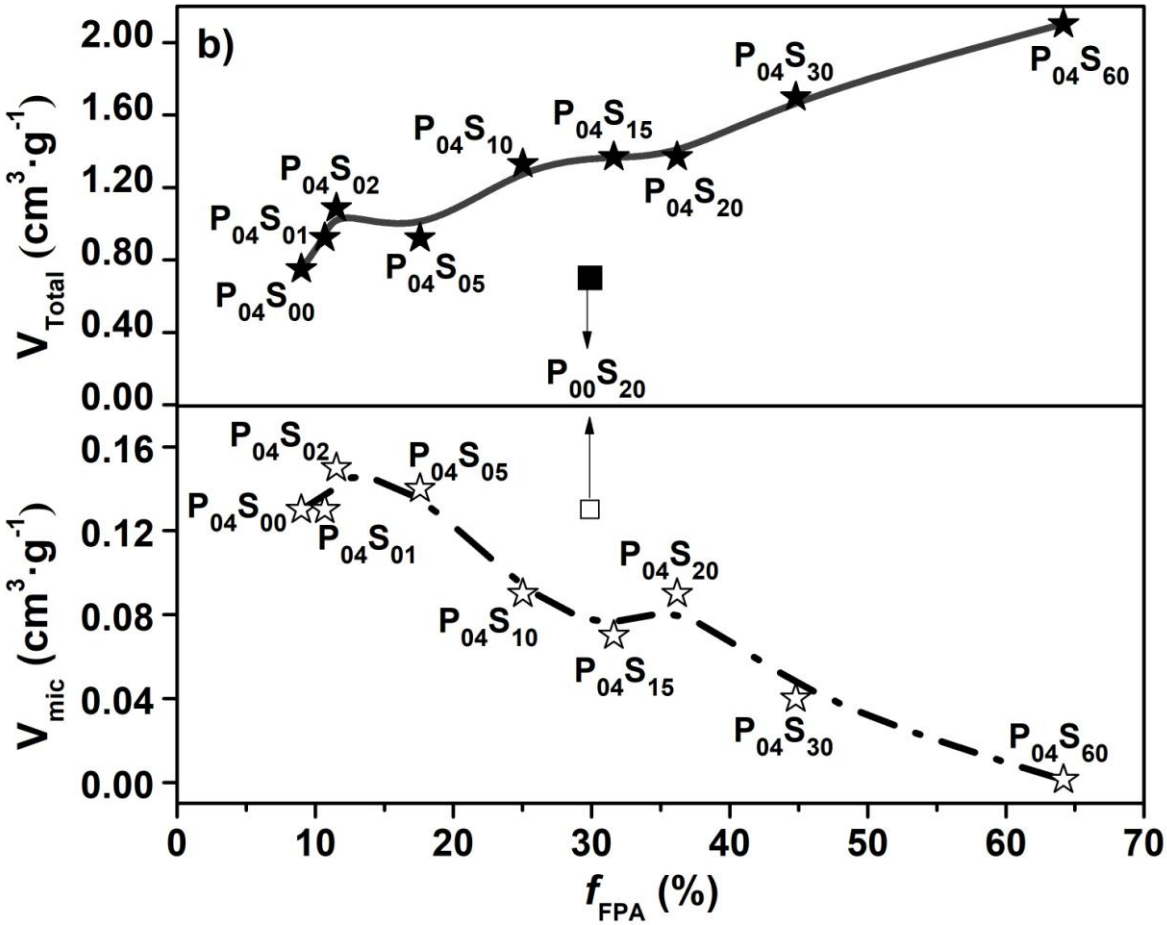
b)
V_{Total} ($cm^3 \cdot g^{-1}$)
V_{mic} ($cm^3 \cdot g^{-1}$)
f_{FPA} (%)
$P_{04}S_{00}$
$P_{04}S_{01}$
$P_{04}S_{02}$
$P_{04}S_{05}$
$P_{04}S_{10}$
$P_{04}S_{15}$
$P_{04}S_{20}$
$P_{04}S_{30}$
$P_{04}S_{60}$
$P_{00}S_{20}$

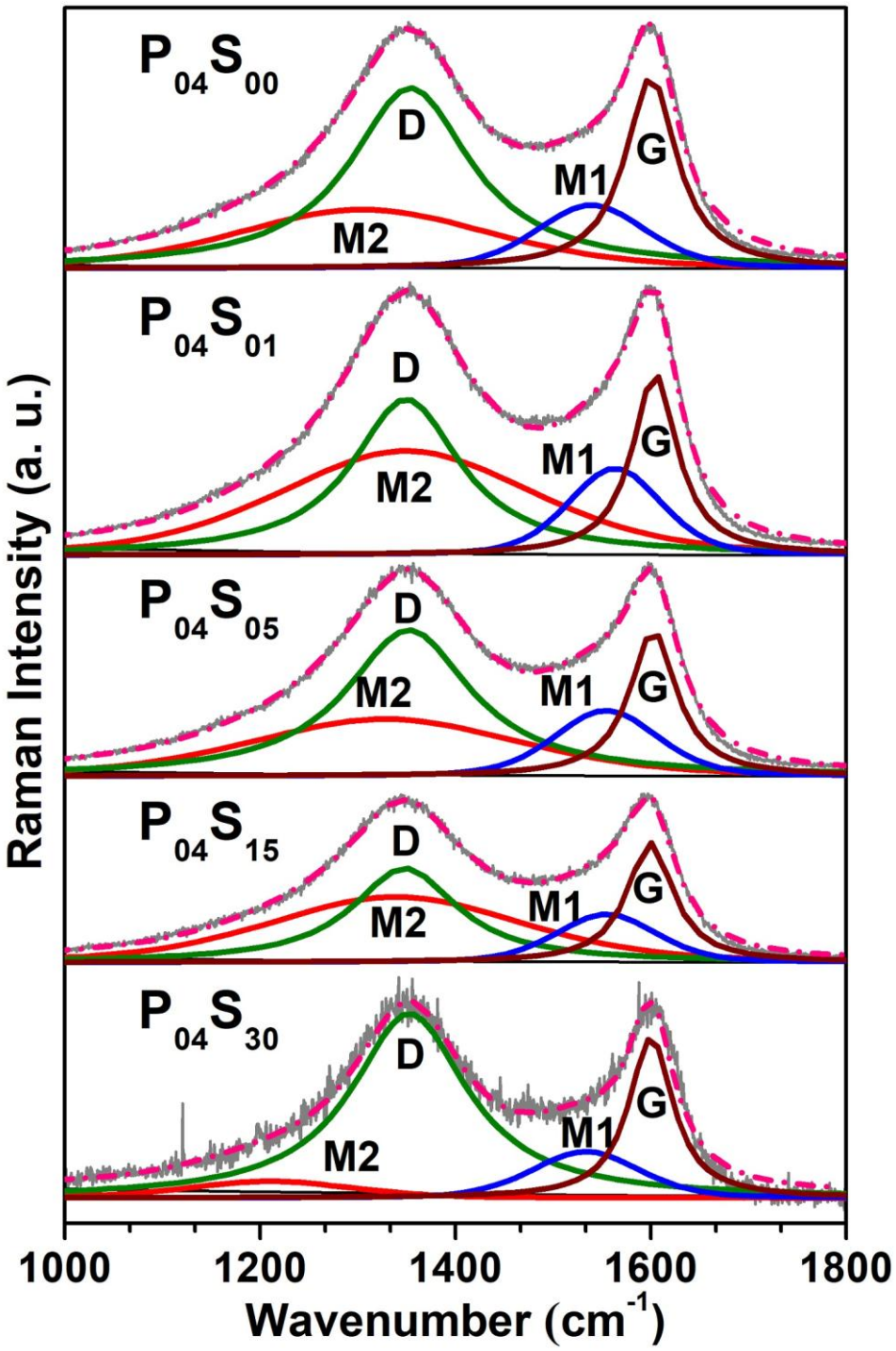
P04S00
D
G
M1
M2
P04S01
D
G
M1
M2
P04S05
D
M2
M1
G
P04S15
D
M2
M1
G
P04S30
D
G
M1
M2
Raman Intensity (a. u.)
1000
1200
1400
1600
1800
Wavenumber (cm-1)

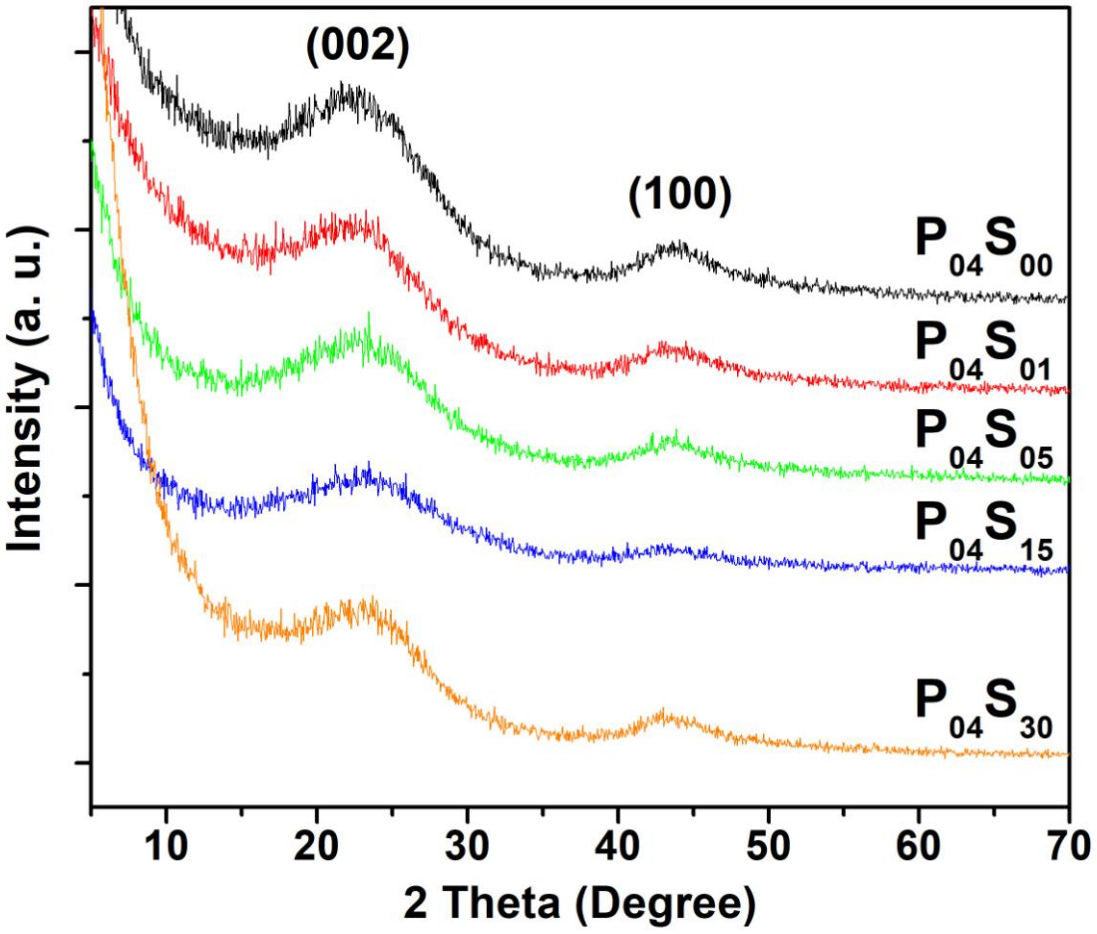
(002)
(100)
P04S00
P04S01
P04S05
P04S15
P04S30
Intensity (a. u.)
10
20
30
40
50
60
70
2 Theta (Degree)

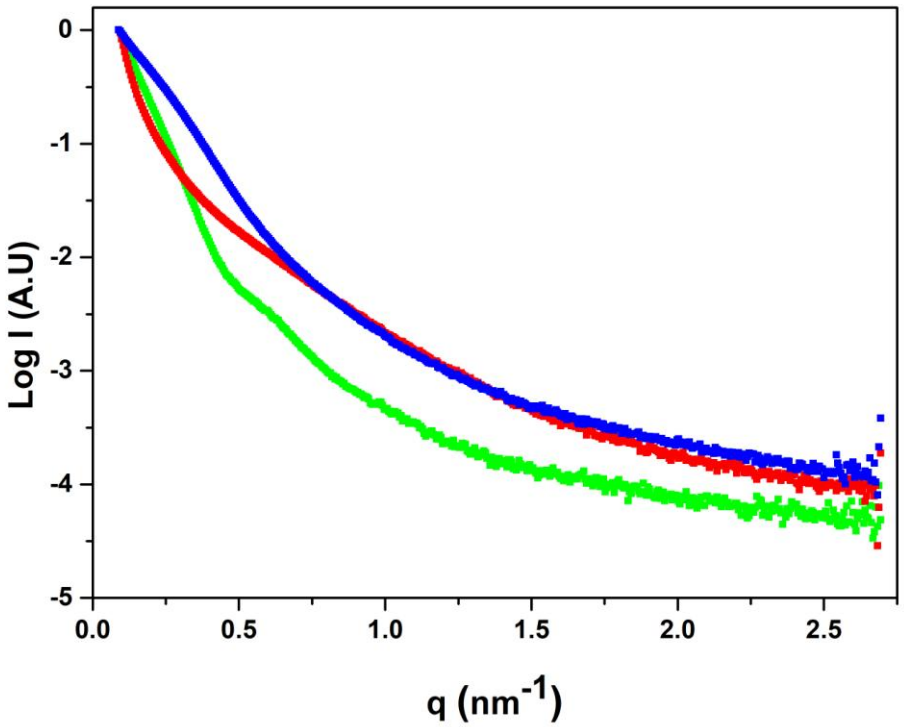

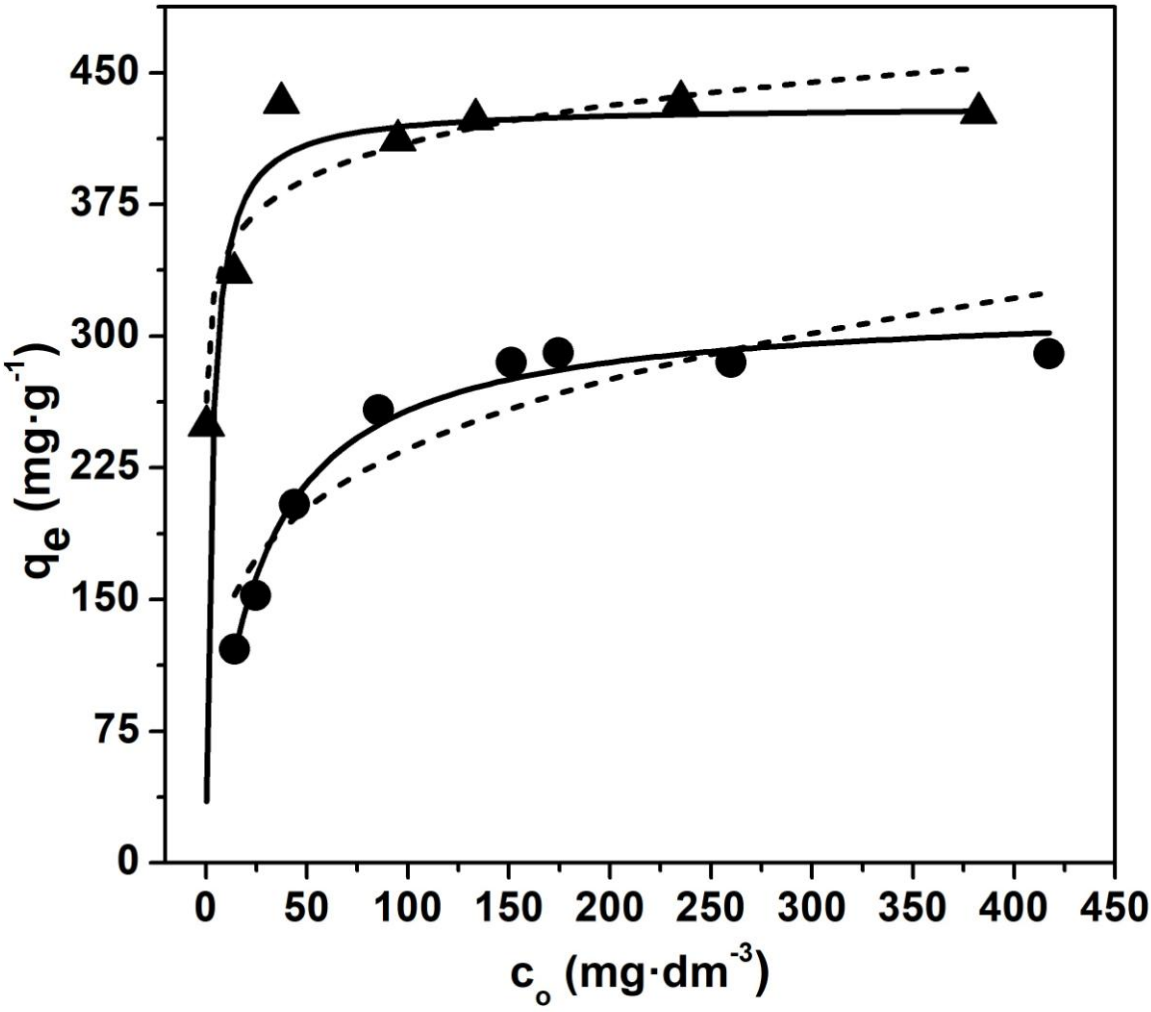
450
375
300
225
150
75
0
q_e (mg·g^{-1})
0
50
100
150
200
250
300
350
400
450
c_o (mg·dm^{-3})

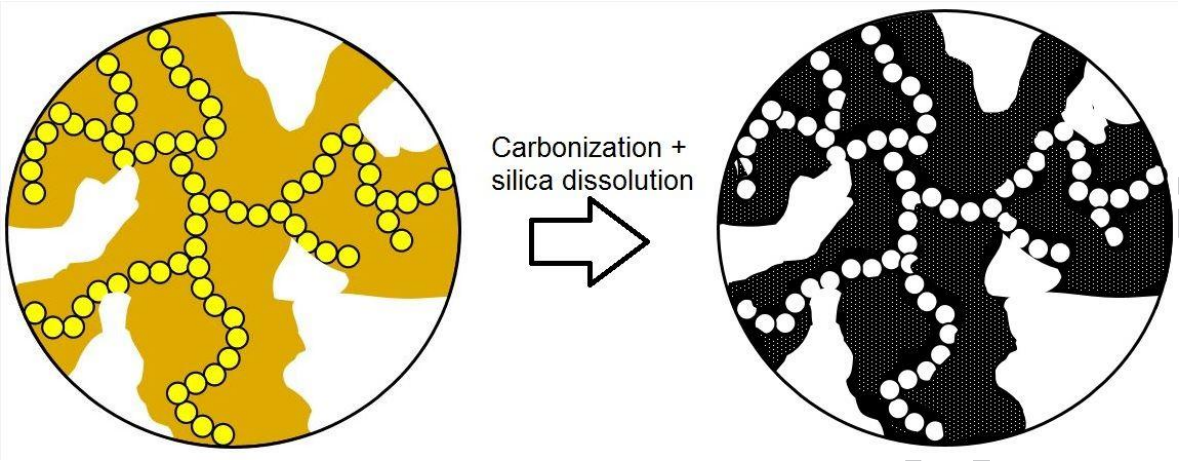

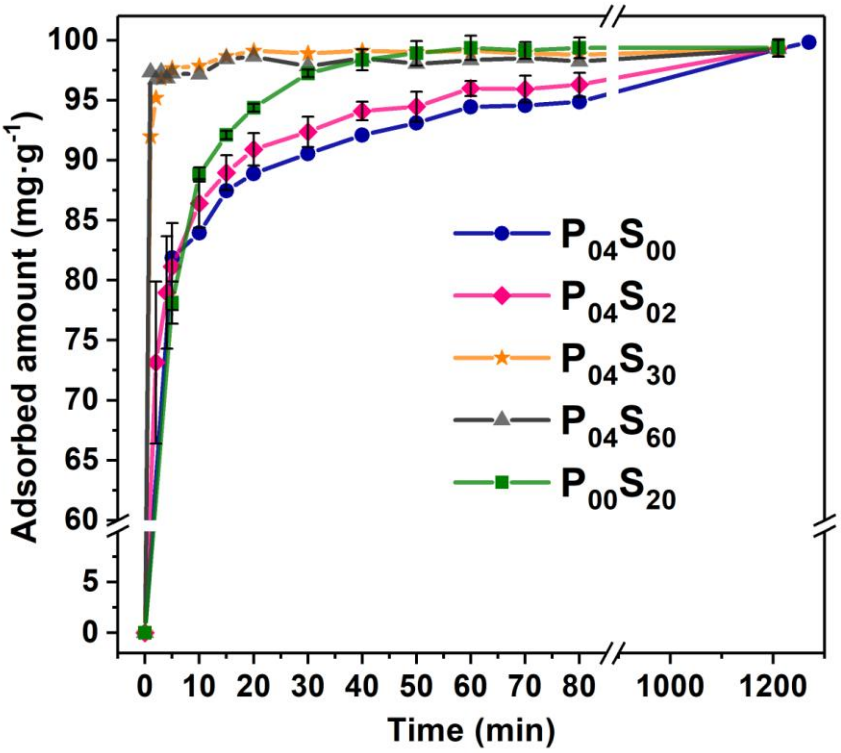

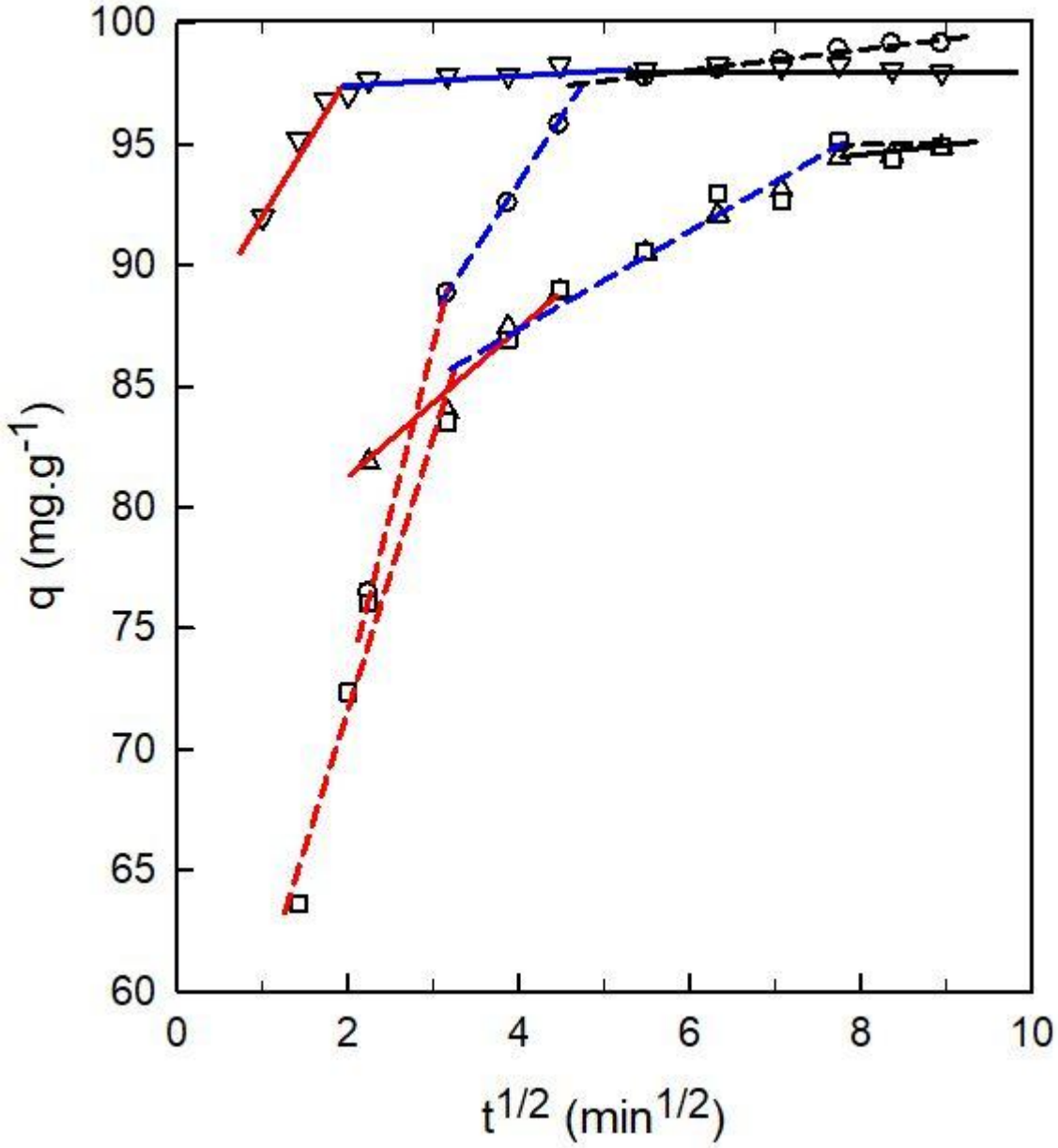
100
95
90
85
80
75
70
65
60
0
2
4
6
8
10
q (mg.g-1)
t1/2 (min1/2)

Graphical Abstract